TECHNISCHE UNIVERSITÄT BERLIN

Institut für Strömungsmechanik und Technische Akustik
Fachgebiet Experimentelle Strömungsmechanik
Prof. Dr.-Ing. C. O. Paschereit

Receptivity analysis of the precessing vortex core in a turbulent swirling jet by open-loop control and adjoint linear stability theory

von

Jens Satria Müller

geboren am 04.01.1991 in Berlin

Masterarbeit zur Erlangung des akademischen Grades

Master of Science

im Studiengang

Luft- und Raumfahrttechnik

Berlin, den 03.04.2018

Matrikelnummer:
331752

Betreuer:
Prof. Dr.-Ing. C. O. Paschereit
Dr.-Ing. K. Oberleithner

Eidesstattliche Erklärung

Hiermit erkläre ich, dass ich die vorliegende Arbeit selbstständig und eigenhändig sowie ohne unerlaubte fremde Hilfe und ausschließlich unter Verwendung der aufgeführten Quellen und Hilfsmittel angefertigt habe.

Berlin, den

.....
Unterschrift

Abstract

The fundamental impact of the precessing vortex core (PVC) as a dominant coherent flow structure in the flow field of swirl-stabilized gas turbine combustors has still not been investigated in depth. In order to do so, the PVC needs to be actively controlled to be able to set its parameters independently to any other of the combustion system. In this work, open-loop actuation is applied in the mixing section between the swirler and the generic combustion chamber of a non-reacting swirling jet setup to investigate the receptivity of the PVC with regard to its lock-in behavior at different streamwise positions. The mean flow in the mixing section as well as in the combustion chamber is measured by stereoscopic particle image velocimetry and the PVC is extracted from the snapshots using proper orthogonal decomposition. The lock-in experiments reveal the axial position in the mixing section that is most suitable for actuation. In addition, the impact of the actuation onto the flow is evaluated and the physical mechanisms leading to lock-in are examined. Furthermore, a global linear stability analysis is conducted to determine the adjoint mode of the PVC which reveals the regions of highest receptivity to periodic actuation based on mean flow input only. This theoretical receptivity model is compared with the experimentally obtained receptivity data and the applicability of the adjoint-based model for the prediction of optimal actuator designs is discussed.

Zusammenfassung

Der Precessing Vortex Core (PVC) ist eine dominante kohärente Struktur im Strömungsfeld von drallstabilisierten Brennkammern in Gasturbinen. Um dessen bis heute noch nicht vollständig untersuchten fundamentalen Einfluss noch tiefgehender zu verstehen, ist es nötig, den PVC aktiv zu kontrollieren, um seine maßgeblichen Parameter unabhängig von allen anderen Parametern der Brennkammer einzustellen. In dieser Arbeit wird ein Aktuator im Mischungsrohr installiert, welches sich zwischen dem Drallerzeuger und der generischen Brennkammer eines nicht-reagierenden Drallstrahls befindet. Durch Open-Loop-Kontrolle wird die Rezeptivität des PVC bezüglich seines Lock-In-Verhaltens an verschiedenen axialen Positionen untersucht. Die mittlere Strömung im Mischungsrohr sowie in der Brennkammer wird durch Stereoscopic Particle Image Velocimetry gemessen und der PVC wird mit Hilfe der Schnappschüsse durch Proper Orthogonal Decomposition extrahiert. Die Ergebnisse der Lock-In-Experimente zeigen, an welcher axialen Position im Mischungsrohr eine Aktuation besonders effektiv ist. Zusätzlich wird der Einfluss der Aktuation auf die Strömung ausgewertet und die physikalischen Mechanismen, die zum Lock-In führen, werden untersucht. Weiterhin wird eine globale lineare Stabilitätsanalyse durchgeführt, um die adjungierte Mode des PVC zu bestimmen. Diese erlaubt es, die Regionen der höchsten Rezeptivität nur anhand des mittleren Strömungsfeldes zu ermitteln. Diese theoretisch berechnete Rezeptivität wird mit der experimentell gemessenen Rezeptivität verglichen und die Anwendbarkeit des Adjungiertenmodells zur Bestimmung von optimalen Aktuatorpositionen wird diskutiert.

Acknowledgment

I want to thank all the colleagues from the department *Experimentelle Strömungsmechanik* for providing an easy but still high level atmosphere, giving me a great place to work in. Special thanks go to Finn Lückoff and Moritz Sieber who were always helpful in providing input and assistance. Furthermore, I want to express my deep gratitude to Dr.-Ing. Kilian Oberleithner who was an excellent supervisor and mentor while conducting my research. He consistently allowed this thesis to be my own work, but at the same time offered valuable guidance whenever I needed it. I would also like to give my acknowledgment to Benjamin Schulz, Nils Demski and my brother Jan Müller for proofreading my thesis and for giving fruitful comments and advice. Finally, I am profoundly grateful to my partner Celine Menjares for providing continuous support through all the years of my studies and during the time of researching and writing this thesis. This work would not have been accomplished without her.

Contents

List of Figures

List of Tables

Nomenclature

a	[m/s]	POD time coefficients
A	[V]	Amplitude
D	[mm]	Tube exit diameter
f	[Hz]	Frequency
$\mathbf{f}$	[m/s^2]	Momentum source (mass-specific)
F	[V]	Forcing oscillation
k'	[m^2/s^2]	Turbulent-stochastic kinetic energy (mass-specific)
$\overline{K}$	[m^4/s^2]	Total mean kinetic energy (mass-specific)
$\widetilde{K}$	[m^4/s^2]	Total coherent kinetic energy (mass-specific)
L	[mm]	Length
m	[−]	Azimuthal wave number
$\dot{m}$	[kg/h]	Mass flow
N	[−]	No. of snapshots
p	[Pa]	Pressure
$\mathbf{q} = (\mathbf{u}, p)$	[m/s], [Pa]	Summarized vector of velocity and pressure
Re	[−]	Reynolds number
S	[−]	Swirl number
$\mathbf{S}$	[1/s]	Strain rate tensor
St	[−]	Strouhal number
t	[s]	Time
T	[s]	Period
u_0	[m/s]	Bulk velocity
$\mathbf{u} = (u, v, w)$	[m/s]	Velocity in (x, y, z) or (x, r, θ) coordinates
V	[−]	Van der Pol oscillation
x_a	[mm]	Axial actuator position
(x, r, θ)	[m], [m], [−]	Cylindrical coordinates (axial, radial, azimuthal)
$\mathbf{x} = (x, y, z)$	[m]	Cartesian coordinates
Γ	[−]	Boundary
λ	[m^2/s^2]	POD mode energy
Λ	[m^2/s^2]	External feedback
μ	[°]	Vane angle
ν, ν_t	[m^2/s]	Kinematic viscosity, eddy viscosity
ω	[Hz]	Angular frequency
φ	[−]	Phase angle
$\mathbf{\Phi}$	[−]	Spatial POD mode
ρ	[kg/m^3]	Density
$\boldsymbol{\tau}$	[Pa]	Stress tensor
χ_t, χ_e	[a.u.]	Theoretical receptivity, experimental receptivity
$\Im(\cdot)$		Imaginary part
$\Re(\cdot)$		Real part
$\langle\cdot\rangle$		Phase-average
$\langle\cdot,\cdot\rangle$		Inner product

$\overline{(\cdot)}$	Mean part
$\widetilde{(\cdot)}$	Coherent part
$(\cdot)'$	Stochastic part
$(\cdot)''$	Fluctuation part
$\hat{(\cdot)}$	Complex amplitude
$(\cdot)^+$	Adjoint
$(\cdot)_f$	Forcing
$(\cdot)_l$	Lock-in
$(\cdot)_n$	Natural
KE	Kinetic Energy
LSA	Linear Stability Analysis
POD	Proper Orthogonal Decomposition
PSD	Power Spectral Density
PVC	Precessing Vortex Core
SP	Stagnation Point
SPIV	Stereoscopic Particle Image Velocimetry
VDP	Van der Pol
ZNMF	Zero Net Mass Flux

1 Introduction

Swirling flows undergoing vortex breakdown have a wide range of application in industrial flows. To understand the physics of these flows and to control these is therefore of great importance. Amongst others, they occur on delta wings at high angle of attack [1], they are exploited for increasing internal cooling performance in turbine blades [2] or they are used for aerodynamically stabilizing the reaction zone of a lean premixed flame in combustion chambers of modern gas turbines [3]. The stabilization is based on the formation of vortex breakdown and the appearance of an inner and outer recirculation zone which act as an anchor for the flame. Vortex breakdown is often accompanied by a dominant coherent structure, the Precessing Vortex Core (PVC). The PVC is a manifestation of a global hydrodynamic instability mode triggered by the reverse flow in the breakdown bubble. It is characterized by a single-helical vortex that meanders downstream around the vortex breakdown bubble.

In recent studies, the impact of the PVC on combustion systems has been investigated. The PVC may alter the flame stability and dynamics [4], it may couple with thermoacoustic instabilities [5–7] or it may influence the mixing of fuel and air [8, 9]. So far, only qualitative trends on these different phenomena could be made out. Nonetheless, the quantitative impact of the PVC is still unclear. The open question remains whether the PVC can be used in a beneficial way to reduce pollutant emissions or increase stability and efficiency.

For a systematical investigation, it is desirable to actively control the PVC in order to set its parameters independently to any other of the combustion system. However, finding a promising actuation concept that works most effectively is a difficult task. Apart from the design of the actuation device itself, numerous flow mechanical factors have to be accounted for. Amongst others, these are the velocity direction the actuator is supposed to actively excite the flow, as well as the definite placement of the device inside the flow field where actuation is applied for maximum control authority at minimum energy input. The way of tackling these problems can be roughly classified into two approaches. On the one hand, various actuation devices with different excitation directions at different positions can be tested in experiments or numerical simulations, covering a very large parameter space. On the other hand, the employment of the mathematical adjoint theory within the scope of the Linear Stability Analysis (LSA) offers an analytical way of solving these problems.

Recently, the LSA of turbulent flows, conducted on the time-averaged mean flow, has been well established as a method for analyzing the PVC. Under the assumption of a parallel or weakly non-parallel flow within the framework of the *local* LSA, Chomaz [10] derived a frequency selection criterion for global modes in spatially developing flows. Gallaire *et al.* [11] proved that this criterion indeed enables the reproduction of the oscillation frequency of a PVC based on data from a direct numerical simulation. Oberleithner *et al.* [12] utilized the local LSA on experimental data and found a good agreement between the spatial modes obtained by local LSA and the modes obtained by Proper Orthogonal Decomposition (POD). Additionally, an excellent match of the predicted frequency of the PVC and the experimentally measured frequency could be demonstrated. Abandoning the parallel flow assumption, the *global* LSA requires much higher computational costs. As these demands are increasingly met, global LSA has found

a wider application in the last decades [13]. Based on experimental data, Paredes *et al.* [14] were able to reproduce the global mode shapes downstream of the mixing section of a combustor with global LSA. Tammisola & Juniper [15] as well as Kaiser *et al.* [16] followed in demonstrating the applicability and validity of global LSA on highly turbulent flows with a dominating PVC instability.

Within the framework of the global LSA, the adjoint mean flow and the adjoint modes have become the focus of interest in guiding future control strategies. They have been used by Giannetti & Luchini [17], Marquet *et al.* [18] and Meliga *et al.* [19, 20] in the context of wake flow vortex shedding of different cylinder geometries to investigate the impact of passive flow control devices on the frequency of the shedding or its suppression. They validated their results to experimental data from Strykowski & Sreenivasan [21], Parezanovic & Cadot [22] and Meliga *et al.* [20] and showed that primarily the adjoint mean flow is contemplable for estimating the impact of these devices. Higher values in the adjoint corresponded to greater changes in the mode when a very small solid body was placed at this particular location. It is interpreted that the impact of a passive control device essentially acts through a steady forcing of the mean flow which in turn changes the modes. Specifically considering active control measures, Magri & Juniper [23] used the adjoint modes to investigate a simple numerical thermoacoustic system comprising a diffusion flame to find regions of the flame which are most receptive to open-loop, i.e. unsteady and periodic, forcing. Furthermore, Tammisola & Juniper [15] obtained the adjoint modes of a PVC outside and inside of a swirl injector based on data from a direct numerical simulation. They showed that the receptivity to open-loop forcing reaches far upstream of the injector. Kaiser *et al.* [16] calculated the adjoint modes of the PVC in a more complex swirl injector geometry based on large eddy simulations. In their case, regions of high receptivity inside the injector were found, too.

In order to control the PVC in an experimental environment, two studies have been recently conducted to find a viable actuator design as well as a promising placement of it. This has been realized in a generic, non-reacting swirling jet setup by Kuhn *et al.* [24]. Active control was exerted by a thin actuator lance within the jet core, exciting or damping the PVC with zero net mass flux (ZNMF) actuation jets introduced radially into the flow. Applying open-loop control, the actuator was traversed along the centerline of the jet with forcing frequencies different to the natural frequency of the PVC. This was done to find positions of high receptivity, i.e. positions where the least amount of input was required to achieve a change of the natural frequency. These were found to be close to the exit of the swirler. At one of these positions, closed-loop control was then exerted to achieve a reduction of the oscillation energy of the PVC by about 40%. One problem of the experiments was the change of the mean flow with different actuation positions due to the passive influence of the actuator. In a consecutive study, Lückoff *et al.* [25] transferred these results to a non-reacting swirling jet of a model combustor. Various actuator designs integrated into a centerbody inside the mixing section of a burner were tested. The external shape of the actuator was kept the same. Each of them introduced axial or radial ZNMF jets. Instead of traversing along different axial positions the actuator was exchanged, thus avoiding an alteration of the mean flow. Again, open-loop control was exerted on the PVC. It was found that both axial and radial forcing close to the exit of the mixing section were highly effective.

The main idea of the present work is to use an actuator upstream of the combustion chamber inlet in a generic swirling jet setup similar to the setup of Kuhn *et al.* [24]. The actuator is implemented into the walls of a mixing section downstream of the swirler and upstream of the chamber inlet. This type of actuator would also be easier to technically apply to industrial conditions since it could be implemented into an already existing

structure without obstructing the flow. Open-loop studies are conducted at different axial positions and the minimum amplitude for frequency lock-in is measured. This produces an experimentally obtained receptivity as a function of the axial coordinate. POD and adjoint modes of an excited case are used to determine a criterion for the adjoint modes to obtain a theoretical receptivity as a function of axial coordinate. This is then used to discuss the validity of the adjoint theory as a model for predicting the receptivity of the PVC to realistic actuation which may guide actuator designs for the active flow control of the PVC in the future. In addition, the mechanisms leading to frequency lock-in and potential changes to the mean flow and the PVC caused by the actuation are investigated.

The PVC mode in the context of its receptivity has only recently been the focus of research, especially upstream of the exit plane of the swirling jet. That is why on the one hand, this thesis is supposed to be complementary to the investigations of Tammisola & Juniper [15] and Kaiser *et al.* [16]. On the other hand, this thesis serves as an *experimental* validation of the physical relevance of the adjoint modes in the context of open-loop control of a PVC and global modes in general. The thesis addresses the following questions: What is the receptivity of the PVC to actuation according to adjoint linear stability theory? Does this theoretically predicted receptivity apply to a measured receptivity obtained by open-loop experiments? What are the physical effects of the open-loop forcing that lead to lock-in?

The present thesis is structured as follows: first, the theoretical methods are introduced. Then, the experimental setup is described including the utilized measurement techniques and data analysis methodology. In the next chapter, the results of the natural, non-forced case are shown at first. This is followed by a comparison to the results from the global LSA. Subsequently, the adjoint modes are calculated, discussed and, eventually, evaluated in comparison to the results from the open-loop studies. Afterwards, the influence of the forcing onto the mean and coherent flow is studied. In the conclusion, all observations are summarized and an outlook is given.

2 Theoretical Concepts

In this chapter, the essential physical concepts and analytical methods which are utilized for the experiment as well as the stability and adjoint analysis are explained.

2.1 Physical Background

In the following section, the fundamental physics of the PVC and its manipulation by open-loop control are described.

2.1.1 Coherent Structures in Turbulent Flows

Until the 1970s, it was a general notion that turbulent flows are predominantly chaotic. Although large-scale organized motions in turbulent shear flows were recognized long before, especially via flow visualization techniques, it was not until the seminal experiments of Crow & Champagne [26] which led to the widespread acceptance that turbulent shear flows consist of orderly quasideterministic structures which are *coherent*, i.e. phase-correlated, over large scales of time and space [27]. One common method to describe these coherent structures is the triple decomposition technique [28]:

$$\mathbf{q}(\mathbf{x},t) = \overline{\mathbf{q}}(\mathbf{x}) + \widetilde{\mathbf{q}}(\mathbf{x},t) + \mathbf{q}'(\mathbf{x},t), \tag{2.1}$$

where $\mathbf{q}$ is an arbitrary space and time dependent quantity of the flow, $\overline{\mathbf{q}}$ is the time-average or mean part, $\widetilde{\mathbf{q}}$ is the coherent fluctuation part (time-average subtracted from phase-average) and $\mathbf{q}'$ is the stochastic fluctuation part. By that, the triple decomposition is basically a refined version of the Reynolds decomposition where all turbulent fluctuations are absorbed into a single fluctuation part $\mathbf{q}'' = \widetilde{\mathbf{q}} + \mathbf{q}'$. The coherent part, on the other hand, quantifies all those structures in the turbulence spectrum which are periodic in time and space.

For open shear flows, such as jets, wakes or mixing layers, the triple decomposition goes along with a separation of scales since the coherent structures feature much larger wavelengths and energy contents compared to the rest of the turbulence spectrum. Consequently, the large-scale coherent structures can be viewed as instability waves which are propagated by a turbulent mean flow with a much larger time-scale than the stochastic background fluctuations of the fine-scale turbulence [12, 29]. These large-scale coherent structures are mainly driven by hydrodynamic instabilities, particularly by the Kelvin-Helmholtz instability [30].

The PVC is a coherent structure and, therefore, typically described with the triple decomposition technique. In case of the PVC, the coherent fluctuation part can be empirically extracted by POD and theoretically modeled by LSA. Both approaches are utilized in this work.

2.1.2 Precessing Vortex Core

A swirling jet is a jet with a vortex core of non-zero mean azimuthal velocity. When the ratio of axial flux of azimuthal momentum to axial flux of axial momentum, quantified

by the swirl number, exceeds a critical value, vortex breakdown occurs. The vortex breakdown is characterized by the emergence of a stagnation point on the jet centerline which leads to deceleration and strong diversion of the flow. Downstream, a recirculation bubble with reverse flow is formed and the radius of the vortex core significantly increases [31]. For swirl numbers slightly above the onset of vortex breakdown, the breakdown is axisymmetric. When a second critical swirl number is exceeded, a global helical instability mode with a dominant characteristic frequency occurs that stems from a local absolute instability inside the recirculation bubble that sets up a feedback cycle and lets the mode grow until it saturates [32]. This leads to the vortex breakdown becoming helical and the vortex core starting to precess in the same direction as the mean flow rotation. This phenomenon is what is known as the PVC. It is a self-excited mode at limit cycle that arises due to a supercritical Hopf bifurcation [33]. The mean flow model is a way to describe the path with which this limit cycle of the global mode is reached: Above the second critical swirl number, a Hopf bifurcation occurs which leads to an absolutely unstable flow with a positive growth rate. Incoming perturbations grow and increase the amplitude of the unstable mode which results in additional coherent Reynolds stresses. These in turn modify the mean flow nonlinearly. The growth rate decreases until the amplitude of the instability saturates and reaches a stable limit cycle. The LSA conducted on the mean flow is then able to predict the frequency of the limit cycle with a corresponding growth rate of zero [34].

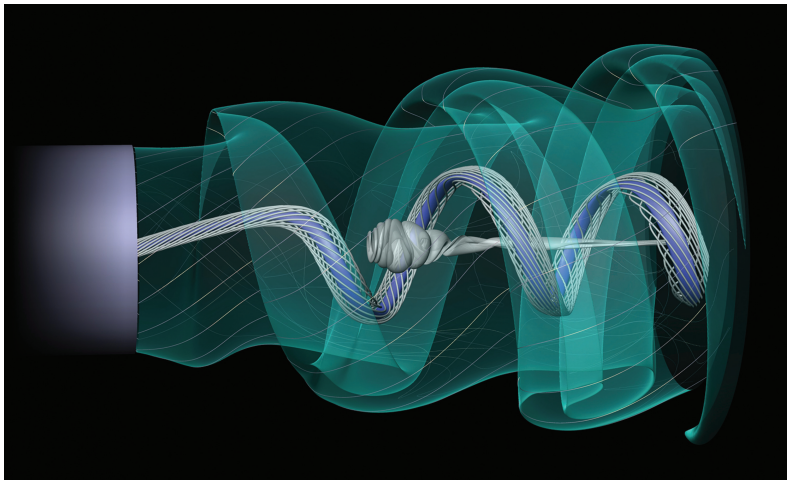

Figure 2.1: Conceptual 3D visualization of the PVC (from Petz *et al.* [35]).

The conceptual topology of the PVC is illustrated in Fig. 2.1, taken from Petz *et al.* [35]. The swirling jet discharges from a nozzle into ambient air from left to right. The eponymous precessing vortex core is displayed by the blue streak surface in the center flowing out from the nozzle in a meandering fashion. The recirculation bubble is shown as a semi-transparent gray pathline surface in the center of the figure. The outer shear layer of the swirling jet is represented by the semi-transparent teal streak surface, depicting the helical Kelvin-Helmholtz instabilities.

2.1.3 Forced Synchronization of Self-Excited Oscillators

The entire following subsection is closely based on the works of Balanov *et al.* [36], if not stated otherwise.

The PVC is a self-excited oscillator. As such, it is fundamentally different to a forced oscillator since it is able to sustain its periodic oscillations without a continuous external periodic forcing. The system needs to be inherently nonlinear to have this ability. It needs to sustain a stable equilibrium between dissipation of energy, i.e. coherent-stochastic Reynolds stresses and viscous stresses in case of the PVC, and supply of energy, i.e. mean flow. A typical feature of a self-excited oscillator is that its frequency, amplitude and mode shape are determined purely by the system's intrinsic properties. In dynamical systems theory, the stable equilibrium nature of the limit cycle of the self-excited oscillator is an attractor in phase space. For any given initial condition, which is sufficiently close to the attractor, the system will asymptotically drift towards its limit cycle. Also, this means that for any finite-time, weakly perturbing deflection from the limit cycle, the system will return to its cycle after a while.

The oscillatory motion of the PVC is nearly harmonic with a characteristic natural frequency. When the system is harmonically perturbed or forced by open-loop control, a phenomenon called frequency synchronization or lock-in may occur where the system stops to oscillate at its natural frequency and starts to oscillate at the forcing frequency instead. For this, the forcing frequency needs to be sufficiently close to the natural frequency of the system, and the forcing amplitude needs to be of sufficient magnitude. In this thesis, only 1:1 forced synchronizations are of interest. This means, that the PVC and the forcing are unidirectionally coupled oscillators: the forcing influences the PVC, but not vice versa; and the synchronized frequency of the system is equal to the forcing frequency instead of a (reciprocal) integer multiple of the forcing frequency.

In the following, a model one-dimensional system with weak nonlinearity is considered, the Van der Pol (VDP) oscillator. The critical forcing amplitude at which the system starts to oscillate stably and in phase with the forcing frequency is called lock-in amplitude. When the lock-in amplitude is plotted against the forcing frequency, the lock-in amplitude A_l is nearly linearly related to the difference between natural frequency f_n and forcing frequency f_f. For a VDP oscillator, $A_l \propto |f_n^2 - f_f^2|$. This nearly linear relation is in general very typical for systems that reached a limit cycle through a Hopf bifurcation [37]. This relation results in the characteristic V-shaped curve of forced self-excited oscillators, the so-called Arnold tongue. In Fig. 2.2 such an Arnold tongue, or lock-in diagram, of a weakly nonlinear VDP oscillator is displayed. The solid and dash-dot line indicate the lock-in amplitude. For forcing frequencies below the solid and dash-dot line (light gray area), the system does not oscillate at the forcing frequency and the system is not locked to the forcing. When the lock-in amplitude is exceeded (dark gray area), the system starts to oscillate at the forcing frequency and the system is locked-in. To illustrate the path to lock-in, three exemplary states as labeled are considered: (a) a natural state which is not forced, (b) a forced, but not locked state (with $f_f/f_n = 0.98$) and (c) a forced and locked-in state.

When the system is in its natural state without being forced, a monofrequency oscillation can be represented by a sinusoidal wave in time domain. Using a Hilbert transform, the real-valued oscillation can be expanded to a complex function which readily defines the phase angle of the oscillator. The phase space is then uniquely determined by plotting the imaginary part $\Im$ of the VDP oscillation $V(t)$ against the real part $\Re$. This phase trajectory gives closed orbits in a two-dimensional plane, as displayed in (a,i) of Fig. 2.3. The closed orbits visually represent the limit cycle of the system. Accordingly, the frequency spectrum shows only one dominant peak at the natural frequency f_n (a,iv). The periodicity of the limit cycle can also be represented with a Poincaré map. For this, a bounded plane transversal to the phase trajectory is defined by $\Im(V) = 0$, as indicated in (a,i). Each time the trajectory intersects this Poincaré section, the state of the system is

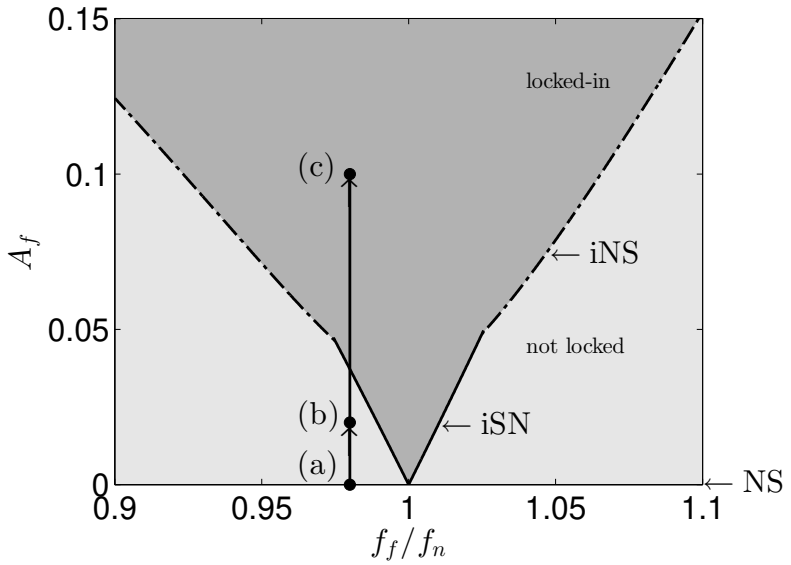

Figure 2.2: Lock-in diagram (Arnold tongue) of a weakly nonlinear VDP oscillator with forcing amplitude A_f over normalized forcing frequency f_f/f_n (light gray: not locked regime; dark gray: locked-in regime; NS: Neimark-Sacker bifurcation, $A_f = 0$; iSN: inverse saddle-node bifurcation, solid line; iNS: inverse Neimark-Sacker bifurcation, dash-dot line).

marked. The Poincaré map shows all of these states for each recurrence of the trajectory to the Poincaré section. When the system is periodic, the phase trajectory will return to the same state after each cycle which corresponds to a stable fixed point in the Poincaré map (a,ii).

Now, when the system is harmonically forced in open-loop by $F(t)$, a third dimension is added to the phase space and the system becomes quasiperiodic through a Neimark-Sacker, or torus birth, bifurcation. The phase trajectory does not lie on a closed orbit anymore but on a torus (b,i). For a fixed forcing value F, the VDP oscillation V takes arbitrary values over time. In other words, F and V oscillate independently of each other. The Poincaré map is a closed curve and the phase trajectory does not return to the same fixed point anymore—the stable fixed point has vanished (b,ii). The difference of the phase angles $\Delta\varphi$ between VDP oscillator φ_{VDP} and forcing φ_f also confirms that both oscillators are not synchronous since both are not in phase (b,iii) and oscillate at their own frequencies (b,iv).

When the forcing amplitude is increased, the diameter of the torus grows at first. The actual route to lock-in can occur in two different ways, however. The first route is the phase lock mechanism which usually occurs when the forcing frequency is very close to the natural frequency (solid line in Fig. 2.2). The natural frequency is gradually 'pulled' [38] towards the forcing frequency when the forcing amplitude is increased. The amplitude of the natural mode is not significantly changed. Lock-in occurs after an inverse saddle-node bifurcation where the torus in the phase space suddenly disappears and a new closed orbit emerges (c,i). This is shown by a new stable fixed point in the Poincaré map, too (c,ii). The phase angle difference between VDP and forcing oscillator is now zero over time (c,iii) and the system oscillates at the forcing frequency (c,iv).

When the forcing frequency is further away from the natural frequency, another route, the suppression mechanism, is taken (dash-dot line in Fig. 2.2). Here, the natural

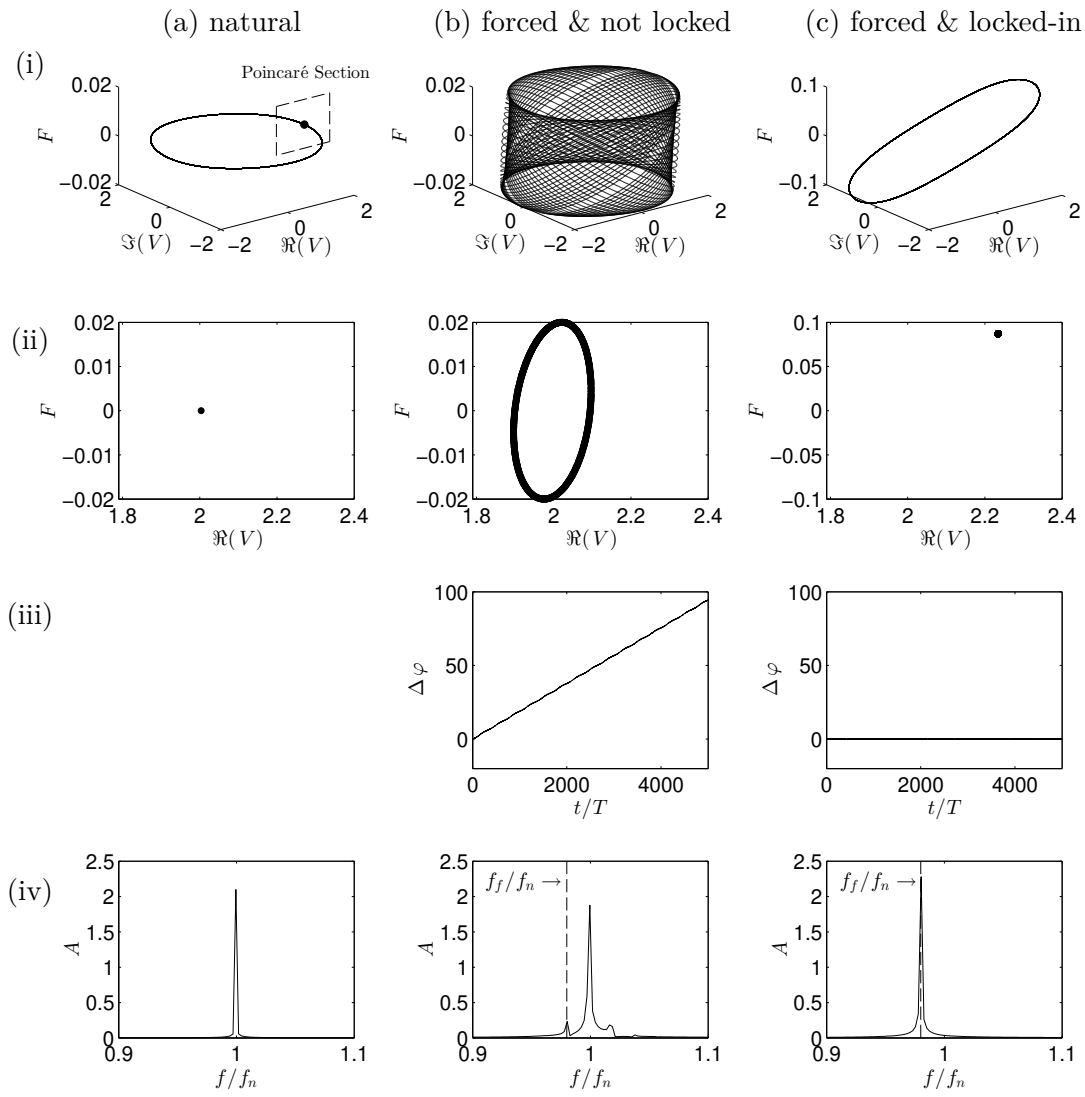

Figure 2.3: Lock-in route of a weakly nonlinear VDP oscillator, (i) phase space: forcing oscillation F over VDP oscillation V, (ii) Poincaré map: forcing oscillation F over real part of VDP oscillation $\Re(V)$ with $\Im(V) = 0$, (iii) phase angle difference $\Delta\varphi$ over normalized time t/T, (iv) frequency spectrum: amplitude A over normalized frequency f/f_n.

frequency stays nearly constant while the natural amplitude is gradually diminished when the forcing amplitude is increased. The torus diameter begins to decrease until it becomes a new closed orbit. Lock-in is reached by an inverse Neimark-Sacker, or torus death, bifurcation. In the Poincaré map, the circular recurrence points converge to a new stable fixed point.

The slope of the Arnold tongue, i.e. whether the V-shape is rather flat or steep, is a function of the system's properties. It characterizes the receptivity of the system to open-loop forcing. A flat tongue means that the system is more receptive to perturbations and more easily brought to a new limit cycle compared to a system with a steeper Arnold tongue. In case of the PVC, the determining parameters are expected to be the Reynolds number, swirl number and the position where the forcing is introduced. Since the exact transfer function between input voltage amplitude and output flow perturbation amplitude is difficult to obtain at flow conditions, the 'effectiveness' of the actuation

device also needs to be factored in. In this thesis, the swirl number will be kept constant and only one actuator will be used. Therefore, at a fixed Reynolds number, the slope of the Arnold tongue will only be a function of the forcing position that directly quantifies the receptivity of the PVC to open-loop forcing at this location.

In this work, open-loop control will be exerted in order to change the frequency of the PVC. As illustrated above, a viable criterion whether lock-in has been reached can be defined by considering the phase angle difference $\Delta\varphi$ between the instantaneous phase of the PVC φ_{PVC} and the phase of the forcing φ_f:

$$\Delta\varphi = \varphi_{\mathrm{PVC}} - \varphi_f + \Delta\varphi_0 \tag{2.2}$$

with $\Delta\varphi_0$ as the initial phase difference at $t = 0$, arbitrarily set to $\Delta\varphi_0 = 0$ here. Lock-in is established when:

$$\Delta\varphi \approx 0, \text{ for } t \to \infty, \tag{2.3}$$

i.e. when the PVC and forcing frequency are approximately equal for the time of measurement. Exact equality is not possible in this highly turbulent setup.

2.2 Analytical Methods

In the following section, the methods which are essential for the empirical and analytical extraction of the PVC as well as the prediction of its receptivity are introduced.

2.2.1 Proper Orthogonal Decomposition

For extracting dominant coherent velocity fluctuations from a turbulent velocity field, the POD is a well tested technique [39]. In the POD, an ensemble of N velocity fields is projected onto an orthogonal N-dimensional basis that maximizes the turbulent kinetic energy for any subspace. Thus, the POD provides an optimal set of modes with which the energy containing structures can be described in the most efficient way with as few modes as possible. The POD of a velocity field $\mathbf{u}$ is then determined with:

$$\mathbf{u}(\mathbf{x}, t) = \overline{\mathbf{u}}(\mathbf{x}) + \sum_{j=1}^{N} a_j(t)\mathbf{\Phi}_j(\mathbf{x}) + \mathbf{u}_{\mathrm{res}}(\mathbf{x}, t) \tag{2.4}$$

by minimizing the residual $\mathbf{u}_{\mathrm{res}}$. The $a_j(t)$ are the POD time coefficients, while the $\mathbf{\Phi}_j(\mathbf{x})$ are the spatial POD modes. In case of Stereoscopic Particle Image Velocimetry (SPIV), N is the number of snapshots. The POD modes $\mathbf{\Phi}_j$ provide the spatial shape of the mode and the time coefficients a_j provide the time dependent amplitude of the modes. Furthermore, the mean specific turbulent kinetic energy of the associated modes can be calculated via $\lambda_j = \overline{a_j^2}$. The POD modes are energy ranked such that $\lambda_1 \geq \lambda_2 \geq \ldots \geq \lambda_N$. In the case of the PVC, the global mode is typically captured by two modes with the highest energy content at similar energy level. Examining the phase portraits of the corresponding time coefficients reveals whether the modes are indeed periodic. When two of such modes occur, the coherent velocity fluctuation of the PVC can be reconstructed by:

$$\widetilde{\mathbf{u}}(\mathbf{x}, t) = \Re\left\{\overline{\sqrt{a_1^2 + a_2^2}}\,\left(\mathbf{\Phi}_1(\mathbf{x}) + \mathrm{i}\cdot\mathbf{\Phi}_2(\mathbf{x})\right) e^{-\mathrm{i}\cdot 2\pi f_{\mathrm{PVC}} t}\right\} \tag{2.5}$$

where $\Re$ is the real part and f_{PVC} is the frequency of the global mode obtained from the Fourier spectra of time-resolved measurements, such as pressure measurements in this work.

2.2.2 Global Linear Stability Analysis

The LSA in turbulent flows is used to obtain modes of coherent velocity fluctuation. In incompressible flows, the governing equations for the hydrodynamic LSA are derived from the incompressible Navier–Stokes equations and the incompressible continuity equation. The triple decomposition ansatz (Eqn. 2.1) is substituted into both equations and both are time-averaged and phase-averaged. By subtracting the time-averaged set of equations from the phase-averaged set of equations, one arrives at the governing equations for the coherent velocity fluctuations [28]:

$$\begin{aligned}\frac{\partial \widetilde{\mathbf{u}}}{\partial t} + \widetilde{\mathbf{u}} \cdot \nabla \overline{\mathbf{u}} + \overline{\mathbf{u}} \cdot \nabla \widetilde{\mathbf{u}} = -\frac{1}{\rho}\nabla \widetilde{p} + \nabla \cdot \left(\nu \left(\nabla + \nabla^{\top} \right) \widetilde{\mathbf{u}} \right) \\ - \nabla \cdot \left(\boldsymbol{\tau}_R + \underbrace{\boldsymbol{\tau}_N}_{\approx 0} \right) \end{aligned} \tag{2.6}$$

$$\nabla \cdot \widetilde{\mathbf{u}} = 0 \tag{2.7}$$

where $\boldsymbol{\tau}_N$ describes the nonlinear interactions between coherent modes. Under the assumption that these interactions are very weak this term is neglected in the following. The term $\boldsymbol{\tau}_R = \langle \mathbf{u}'\mathbf{u}' \rangle - \overline{\mathbf{u}'\mathbf{u}'} = \widetilde{\mathbf{u}'\mathbf{u}'}$ describes the fluctuation of the stochastic Reynolds stresses due to the passage of a coherent perturbation [28]. This term has to be modeled in order to close Eqn. 2.6. In the context of the LSA in swirling flows with a PVC, it is now well established to use Boussinesq's eddy viscosity model as a closure [14–16, 40]. This is done here as well. It is also usually assumed that the coherent fluctuations of the turbulent kinetic energy are small enough to be negligible [28] (in this experiment, it is ascertained to be valid since the coherent fluctuations are smaller than 10%). With that assumption one arrives at:

$$\boldsymbol{\tau}_R = \widetilde{\mathbf{u}'\mathbf{u}'} = -\nu_t (\nabla + \nabla^{\top}) \widetilde{\mathbf{u}}. \tag{2.8}$$

The unknown eddy viscosity is calculated from the known velocity field of the experiment. As the turbulence of the swirling jet is highly anisotropic [40], the approach in Eqn. 2.8 yields six independent eddy viscosities. A reasonable compromise among the six eddy viscosities can be achieved by using a least-square fit over all resolved stochastic Reynolds stresses [41]:

$$\nu_t = \frac{\left\langle -\overline{\mathbf{u}'\mathbf{u}'} + 2/3 \cdot k' \mathbf{I} \, , \, \overline{\mathbf{S}} \right\rangle_{\mathrm{F}}}{2 \left\langle \overline{\mathbf{S}} \, , \, \overline{\mathbf{S}} \right\rangle_{\mathrm{F}}} \tag{2.9}$$

where $\langle \cdot \, , \, \cdot \rangle_{\mathrm{F}}$ is the Frobenius inner product, k' is the turbulent-stochastic kinetic energy, $\mathbf{I}$ is the identity tensor and $\overline{\mathbf{S}} = 1/2 \cdot (\nabla + \nabla^{\top}) \overline{\mathbf{u}}$ is the mean strain rate tensor. The eddy viscosity is then simply added to the kinematic viscosity in Eqn. 2.6 to form an effective viscosity $\nu_{\mathrm{eff}} = \nu + \nu_t$. The linearized Navier–Stokes and continuity equation for the coherent fluctuation become:

$$\frac{\partial \widetilde{\mathbf{u}}}{\partial t} + \widetilde{\mathbf{u}} \cdot \nabla \overline{\mathbf{u}} + \overline{\mathbf{u}} \cdot \nabla \widetilde{\mathbf{u}} = -\frac{1}{\rho}\nabla \widetilde{p} + \nabla \cdot \left(\nu_{\mathrm{eff}} \left(\nabla + \nabla^{\top} \right) \widetilde{\mathbf{u}} \right) \tag{2.10}$$

$$\nabla \cdot \widetilde{\mathbf{u}} = 0. \tag{2.11}$$

These equations can be rewritten to:

$$\mathcal{B}\frac{\partial\widetilde{\mathbf{q}}}{\partial t} - \mathcal{A}\widetilde{\mathbf{q}} = 0 \tag{2.12}$$

where $\mathcal{A}$ and $\mathcal{B}$ represent the operators of Eqn. 2.10 and 2.11 and $\widetilde{\mathbf{q}} = [\widetilde{\mathbf{u}}, \widetilde{p}]^\top$ is the summarized vector of the velocities and pressure.

The global LSA examines flows which are inhomogeneous in two or three spatial dimensions. These are typically named bi-global and tri-global LSA. Within the scope of the PVC, a bi-global analysis suffices due to the homogeneity along the azimuthal direction. Equation 2.12 is solved with a normal mode ansatz in cylindrical coordinates:

$$\widetilde{\mathbf{q}}(\mathbf{x}, t) = \Re\left\{\hat{\mathbf{q}}(x, r)e^{\mathrm{i}(m\theta - \omega t)}\right\} \tag{2.13}$$

where m is the azimuthal wave number and ω is the complex angular frequency. Since the PVC is a single-helical mode, the azimuthal wave number is set to $m = 1$. Discretization and rearrangement lead to a generalized eigenvalue problem with ω as the eigenvalue which can be written in the form of [42]:

$$\mathbf{A}\hat{\mathbf{q}} = \omega\mathbf{B}\hat{\mathbf{q}} \tag{2.14}$$

in which $\mathbf{A}$ and $\mathbf{B}$ are the discretized operators of Eqn. 2.12, including Eqn. 2.13. Solving Eqn. 2.14 provides the eigenmodes $\hat{\mathbf{q}}$, each accompanied with one complex eigenvalue, respectively. It consists of a real part $\Re(\omega)$ that corresponds to the angular frequency of the mode and an imaginary part $\Im(\omega)$ that corresponds to the growth rate of the mode. The mode is stable when $\Im(\omega) < 0$, marginally stable when $\Im(\omega) = 0$ and unstable when $\Im(\omega) > 0$. In the eigenspectrum, an oscillator mode at limit cycle such as the PVC is expected to be an eigenvalue isolated from any continuous eigenvalue branch and ideally marginally stable ($\Im(\omega) = 0$) since the instability neither grows nor decays [34]. With that criterion and the known frequency from the experiment, the PVC mode can be identified and written as:

$$\widetilde{\mathbf{u}}(\mathbf{x}, t) = \Re\left\{\hat{\mathbf{u}}(x, r)e^{\mathrm{i}(\theta - \Re(\omega)t)}\right\}. \tag{2.15}$$

2.2.3 Adjoint Global Linear Stability Analysis

The adjoint global LSA will be employed to estimate the receptivity of the PVC. In order to understand why the adjoint theory is so useful, a small mathematical excursion is ventured. First, the so-called biorthogonality condition will be derived which will in turn help to derive a concrete interpretation of the adjoint modes.

The discrete formulation of the generalized eigenvalue problem of Eqn. 2.14 solves for the right eigenvectors $\hat{\mathbf{q}}$. The problem can also be reformulated and solved for the left eigenvectors $\hat{\mathbf{q}}^+$ instead:

$$(\hat{\mathbf{q}}^+)^{\mathrm{H}}\mathbf{A} = \omega(\hat{\mathbf{q}}^+)^{\mathrm{H}}\mathbf{B} \tag{2.16}$$

$$\Leftrightarrow \mathbf{A}^{\mathrm{H}}\hat{\mathbf{q}}^+ = \omega^+\mathbf{B}^{\mathrm{H}}\hat{\mathbf{q}}^+ \tag{2.17}$$

where $(\cdot)^{\mathrm{H}}$ denotes a Hermitian transpose, i.e. transpose with complex conjugate entries, and $(\cdot)^+$ denotes an adjoint quantity (note that $\omega^+ = \omega^{\mathrm{H}}$). Equation 2.17 is called the adjoint eigenvalue problem [43]. In case of a converged adjoint solution, the adjoint

eigenvalue ω^+ of the PVC is the complex conjugate of the direct eigenvalue ω. By that, the adjoint eigenmode can be identified.

The Hermitian inner product on a complex vector space is defined by $\langle \mathbf{Mx}, \mathbf{y} \rangle = (\mathbf{Mx})^{\mathrm{H}}\mathbf{y} = \langle \mathbf{x}, \mathbf{M}^{\mathrm{H}}\mathbf{y} \rangle$ [44]. Let $\hat{\mathbf{q}}_k$ be an eigenvector to the kth eigenvalue of the direct eigenvalue problem from Eqn. 2.14 and $\hat{\mathbf{q}}_j^+$ be an adjoint eigenvector to the jth adjoint eigenvalue of the adjoint eigenvalue problem from Eqn. 2.17. Contracting the direct problem in Eqn. 2.14 with $\hat{\mathbf{q}}_j^+$ and contracting the adjoint problem in Eqn. 2.17 with $\hat{\mathbf{q}}_k$ by using the Hermitian inner product one arrives at:

$$\langle \mathbf{A}\hat{\mathbf{q}}_k, \hat{\mathbf{q}}_j^+ \rangle = \langle \omega_k \, \mathbf{B}\hat{\mathbf{q}}_k, \hat{\mathbf{q}}_j^+ \rangle \tag{2.18}$$

$$\langle \mathbf{A}^{\mathrm{H}}\hat{\mathbf{q}}_j^+, \hat{\mathbf{q}}_k \rangle = \langle \omega_j^+ \, \mathbf{B}^{\mathrm{H}}\hat{\mathbf{q}}_j^+, \hat{\mathbf{q}}_k \rangle \, . \tag{2.19}$$

Equation 2.18 can be rewritten to:

$$\langle \hat{\mathbf{q}}_j^+, \mathbf{A}\hat{\mathbf{q}}_k \rangle = \langle \hat{\mathbf{q}}_j^+, \omega_k \, \mathbf{B}\hat{\mathbf{q}}_k \rangle \tag{2.20}$$

and Eqn. 2.19 to:

$$\langle \hat{\mathbf{q}}_j^+, \mathbf{A}\hat{\mathbf{q}}_k \rangle = \langle \hat{\mathbf{q}}_j^+, (\omega_j^+)^{\mathrm{H}} \, \mathbf{B}\hat{\mathbf{q}}_k \rangle. \tag{2.21}$$

Subtracting Eqn. 2.21 from Eqn. 2.20 yields:

$$(\omega_k - (\omega_j^+)^{\mathrm{H}}) \langle \hat{\mathbf{q}}_j^+, \mathbf{B}\hat{\mathbf{q}}_k \rangle = 0. \tag{2.22}$$

This is the biorthogonality condition [43]. If $k = j$, the expression inside the round brackets vanishes since $\omega_{k=j} = (\omega_j^+)^{\mathrm{H}}$. If $k \neq j$, it directly follows that $\langle \hat{\mathbf{q}}_j^+, \mathbf{B}\hat{\mathbf{q}}_k \rangle = 0$. Hence, the direct and adjoint eigenvectors are biorthogonal with regard to $\mathbf{B}$ except if $k = j$. This important property will be used in the following to derive a useful interpretation of the adjoint eigenvectors, closely based on the work of Chandler [45].

The linearized Navier–Stokes equation for the coherent fluctuation (Eqn. 2.12) is a homogeneous initial value problem which needs to be supplied with an initial condition $\widetilde{\mathbf{q}}(t = 0) = \hat{\mathbf{q}}_0$. It describes the temporal evolution of the coherent flow. When only normal modes are considered, the solutions of the discretized version of Eqn. 2.12 are given by solving the corresponding eigenvalue problem of Eqn. 2.14. Now, a momentum source $\widetilde{\mathbf{f}} = \hat{\mathbf{f}} e^{\mathrm{i}(\theta - \omega_f t)}$ as an external harmonic, helical forcing is added on the right hand side, which is assumed to not interact with the system. Hence, the spectrum is not modified by the source and can be interpreted as an open-loop source term. The initial value problem can then be written as an inhomogeneous partial differential equation:

$$\mathcal{B}\frac{\partial \widetilde{\mathbf{q}}}{\partial t} - \mathcal{A}\widetilde{\mathbf{q}} = \hat{\mathbf{f}} e^{\mathrm{i}(\theta - \omega_f t)}. \tag{2.23}$$

The general discrete solution is

$$\widetilde{\mathbf{q}} = \widetilde{\mathbf{q}}_h + \widetilde{\mathbf{q}}_p, \tag{2.24}$$

i.e. the sum of the homogeneous and the particular solution. The homogeneous solution is given by the solution of the generalized eigenvalue problem (Eqn. 2.14) and can be written as the superposition of every eigenmode:

$$\widetilde{\mathbf{q}}_h = \sum_{j=1}^{N} \alpha_j \hat{\mathbf{q}}_j e^{\mathrm{i}(\theta-\omega_j t)} \tag{2.25}$$

with yet unknown coefficients α_j. In order to find the particular solution an ansatz which is of the form of the right hand side of Eqn. 2.23 is made:

$$\widetilde{\mathbf{q}}_p = \hat{\mathbf{q}}_p e^{\mathrm{i}(\theta-\omega_f t)}. \tag{2.26}$$

Substituting the ansatz into the inhomogeneous partial differential equation (Eqn. 2.23) and discretizing gives:

$$(\omega_f \mathbf{B} - \mathbf{A})\hat{\mathbf{q}}_p = \hat{\mathbf{f}}. \tag{2.27}$$

If the eigenvectors form a complete set, i.e. a basis, the particular solution $\hat{\mathbf{q}}_p$ and the initial condition $\hat{\mathbf{q}}_0$ can be projected onto that basis and be expressed with the direct eigenvectors $\hat{\mathbf{q}}_j$ as the basis:

$$\hat{\mathbf{q}}_p = \sum_{j=1}^{N} \beta_j \hat{\mathbf{q}}_j \tag{2.28}$$

$$\hat{\mathbf{q}}_0 = \sum_{j=1}^{N} \gamma_j \hat{\mathbf{q}}_j. \tag{2.29}$$

Now, taking the inner product of an adjoint mode $\hat{\mathbf{q}}_j^+$ with Eqn. 2.27 leads to:

$$\langle \hat{\mathbf{q}}_j^+, \omega_f \mathbf{B}\hat{\mathbf{q}}_p \rangle - \langle \hat{\mathbf{q}}_j^+, \mathbf{A}\hat{\mathbf{q}}_p \rangle = \langle \hat{\mathbf{q}}_j^+, \hat{\mathbf{f}} \rangle. \tag{2.30}$$

Substituting the projected $\hat{\mathbf{q}}_p$ from Eqn. 2.28 into Eqn. 2.30 , recalling that $\mathbf{A}\hat{\mathbf{q}}_j = \omega_j \mathbf{B}\hat{\mathbf{q}}_j$ from Eqn. 2.14 and using the biorthogonality condition from Eqn. 2.22 gives:

$$\langle \hat{\mathbf{q}}_j^+, \omega_f \beta_j \mathbf{B}\hat{\mathbf{q}}_j \rangle - \langle \hat{\mathbf{q}}_j^+, \omega_j \beta_j \mathbf{B}\hat{\mathbf{q}}_j \rangle = \langle \hat{\mathbf{q}}_j^+, \hat{\mathbf{f}} \rangle, \tag{2.31}$$

and for the coefficients β_j one obtains:

$$\beta_j = \frac{1}{\omega_f - \omega_j} \frac{\langle \hat{\mathbf{q}}_j^+, \hat{\mathbf{f}} \rangle}{\langle \hat{\mathbf{q}}_j^+, \mathbf{B}\hat{\mathbf{q}}_j \rangle}. \tag{2.32}$$

In a similar fashion, the coefficients γ_j for the initial condition can be found by taking the inner product of an adjoint eigenmode $\hat{\mathbf{q}}_j^+$ and Eqn. 2.29, premultiplied with $\mathbf{B}$, and again utilizing the biorthogonality condition of Eqn. 2.22:

$$\gamma_j = \frac{\langle \hat{\mathbf{q}}_j^+, \mathbf{B}\hat{\mathbf{q}}_0 \rangle}{\langle \hat{\mathbf{q}}_j^+, \mathbf{B}\hat{\mathbf{q}}_j \rangle}. \tag{2.33}$$

Applying the initial condition at $t = 0$ for Eqn. 2.24 and substituting Eqn. 2.25, 2.28 and 2.29 produces:

$$\alpha_j = \gamma_j - \beta_j = \frac{\langle \hat{\mathbf{q}}_j^+, \mathbf{B}\hat{\mathbf{q}}_0 \rangle}{\langle \hat{\mathbf{q}}_j^+, \mathbf{B}\hat{\mathbf{q}}_j \rangle} - \frac{1}{\omega_f - \omega_j} \frac{\langle \hat{\mathbf{q}}_j^+, \hat{\mathbf{f}} \rangle}{\langle \hat{\mathbf{q}}_j^+, \mathbf{B}\hat{\mathbf{q}}_j \rangle}. \tag{2.34}$$

Eventually, the inhomogeneous discrete solution of Eqn. 2.23 can be written as:

$$\widetilde{\mathbf{q}} = \sum_{i=1}^{N} \left\langle \hat{\mathbf{q}}_j^+, \mathbf{B}\hat{\mathbf{q}}_0 e^{\mathrm{i}(\theta-\omega_j t)} + \hat{\mathbf{f}} \frac{e^{\mathrm{i}(\theta-\omega_f t)} - e^{\mathrm{i}(\theta-\omega_j t)}}{\omega_f - \omega_j} \right\rangle \frac{\hat{\mathbf{q}}_j}{\langle \hat{\mathbf{q}}_j^+, \mathbf{B}\hat{\mathbf{q}}_j \rangle}. \tag{2.35}$$

Now, let $\hat{\mathbf{q}}_1$ be the eigenmode of the PVC. When oscillating at limit cycle, the growth rate is zero ($\Im(\omega_1) = 0$), as argued above. Furthermore, all remaining modes are decaying with $\Im(\omega_{j\neq 1}) < 0$. Also, the forcing is assumed to be of constant amplitude, thus $\Im(\omega_f) = 0$. For t becoming very large, the solution of Eqn. 2.35 can then be rewritten to:

$$\begin{aligned} \widetilde{\mathbf{q}} = \frac{\langle \hat{\mathbf{q}}_1^+, \mathbf{B}\hat{\mathbf{q}}_0 \rangle}{\langle \hat{\mathbf{q}}_1^+, \mathbf{B}\hat{\mathbf{q}}_1 \rangle} \hat{\mathbf{q}}_1 e^{\mathrm{i}(\theta-\omega_1 t)} &- \frac{\langle \hat{\mathbf{q}}_1^+, \hat{\mathbf{f}} \rangle}{(\omega_f - \omega_1)\langle \hat{\mathbf{q}}_1^+, \mathbf{B}\hat{\mathbf{q}}_1 \rangle} \hat{\mathbf{q}}_1 e^{\mathrm{i}(\theta-\omega_1 t)} \\ &+ \frac{\langle \hat{\mathbf{q}}_1^+, \hat{\mathbf{f}} \rangle}{(\omega_f - \omega_1)\langle \hat{\mathbf{q}}_1^+, \mathbf{B}\hat{\mathbf{q}}_1 \rangle} \hat{\mathbf{q}}_1 e^{\mathrm{i}(\theta-\omega_f t)}, \end{aligned} \tag{2.36}$$

or abbreviated:

$$\widetilde{\mathbf{q}} = \hat{\mathbf{q}}_1 [(R_0 - R_f) \cdot e^{\mathrm{i}(\theta-\omega_1 t)} + R_f \cdot e^{\mathrm{i}(\theta-\omega_f t)}], \tag{2.37}$$

with

$$R_0 = \frac{\langle \hat{\mathbf{q}}_1^+, \mathbf{B}\hat{\mathbf{q}}_0 \rangle}{\langle \hat{\mathbf{q}}_1^+, \mathbf{B}\hat{\mathbf{q}}_1 \rangle} \tag{2.38}$$

$$R_f = \frac{\langle \hat{\mathbf{q}}_1^+, \hat{\mathbf{f}} \rangle}{(\omega_f - \omega_1)\langle \hat{\mathbf{q}}_1^+, \mathbf{B}\hat{\mathbf{q}}_1 \rangle}. \tag{2.39}$$

The resulting spatial mode shape of the system is not altered by the forcing and, in the limit of t becoming very large, is the PVC mode $\hat{\mathbf{q}}_1$ itself. The temporal response of the system is, however, decomposed into three contributions whose amplitudes are proportional to the magnitude of $|R_0|$ or $|R_f|$, respectively. The response of the system due to the initial condition $\hat{\mathbf{q}}_0$ is at the PVC frequency ω_1 and proportional to $|R_0|$. $|R_0|$ increases when the spatial structure of the initial condition $\hat{\mathbf{q}}_0$ approaches the spatial structure of the adjoint PVC mode $\hat{\mathbf{q}}_1^+$. The response of the system due to the forcing is both at the PVC frequency ω_1 and at the forcing frequency ω_f. Their amplitudes are proportional to $|R_f|$ which increases when the spatial structure of the forcing $\hat{\mathbf{f}}$ approaches the spatial structure of the adjoint PVC mode $\hat{\mathbf{q}}_1^+$. Additionally, $|R_f|$ increases when the forcing frequency ω_f approaches the PVC frequency ω_1. Therefore, the magnitude of the adjoint mode $|\hat{\mathbf{q}}_1^+|$ can be physically interpreted as the receptivity of the system to a given initial condition and to a given open-loop forcing.

Clearly, the typical, nearly linear lock-in behavior for forced synchronization can be seen here as well. For a given PVC, there is one adjoint mode and the receptivity is fixed. Then, to achieve the same response of the system, it follows that $|\hat{\mathbf{f}}| \propto |\omega_f - \omega_1|$, i.e. the forcing amplitude needs to be larger for forcing frequencies differing further from the natural frequency. This corresponds to the Arnold tongue explained in Sec. 2.1.3.

Furthermore, Eqn. 2.37 describes two simultaneously existing oscillators. Hence, the resulting oscillation is quasiperiodic, analog to the system's response of a forced self-excited oscillator after a Neimark-Sacker bifurcation. In the phase space the system is then also represented by a torus.

It has to be emphasized that Eqn. 2.12 describes a *linear* dynamical system. The equation is only used to describe the PVC in its limit cycle by linearizing around the mean flow (see Sec. 2.1.2). It does not describe how the PVC state is reached starting from an arbitrary initial condition, since the phase trajectory that reaches the limit cycle in the phase space is dictated by nonlinear effects (see Sec. 2.1.3). This also explains why the initial condition has a non-zero influence in the time-asymptotic limit since there is no nonlinear mechanism that absorbs initial perturbations. This does not conform to reality, of course. However, since a linearized dynamical equation is examined, it can be assumed that the linear solution at least provides an acceptable estimate of the system's response for sufficiently small perturbations. The adjoint theory has, therefore, its limits within this assumption, and will only give a gradient-like estimation but not a full description of the synchronization process such as the dynamical systems theory will (as seen in Sec. 2.1.3). Still, the goal of this thesis is to show that this linear approach is still sufficient to provide valuable estimates.

3 Experimental and Numerical Setup

In this section, the experimental setup of the swirling jet facility including the ZNMF actuator is illustrated. Furthermore, the utilized measurement techniques are explained.

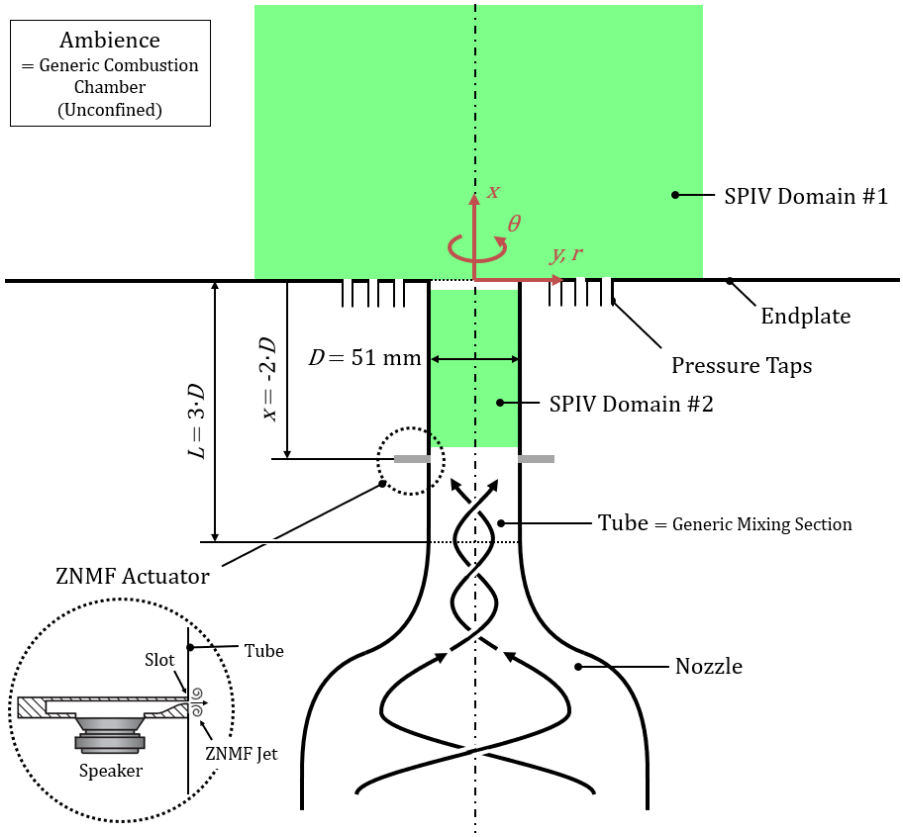

Figure 3.1: Experimental setup, sectional view, with SPIV domains and actuator position $x_a/D = -2$ (speaker graphic from Oberleithner [33]).

In Fig. 3.1 a sketch of the overall experimental setup is shown in a sectional view. In the figure, the swirling flow is depicted moving from bottom to top. The swirl is introduced upstream of the nozzle by radial vanes whose angle can be adjusted continuously (further details in [24]). Downstream of the swirler, the flow goes through the nozzle with an area contraction ratio of 9.1 and then enters a tube of constant diameter $D = 51\,\text{mm}$ and of length $L = 153\,\text{mm}$, which equals three tube diameters. The flow then exits the tube and emanates into unconfined ambient air. The exit plane is bordered by an endplate. At the intersection of the exit plane with the tube axis lies the origin of the coordinate system with x pointing in the direction of the main flow and y and z being orthogonal. In this thesis, the Cartesian coordinates y and z will be sometimes used interchangeably with the cylindrical coordinates r (radius) and θ (azimuth). The tube represents the generic mixing section of a combustor with a premixed flame while the area downstream of the tube corresponds to the flow field inside a combustion chamber.

For the open-loop control of the PVC, eight ZNMF actuation units are used as employed by Oberleithner [33], capable of exciting azimuthal modes of $m = 0$ to 4. Each unit consists of one loudspeaker with a rated input power of 15 W connected by small channels to the tube duct, as sketched in Fig. 3.1. Each stroke period of the speaker creates a ZNMF jet at the slot exit of the actuator channel with a rectangular cross-section of 1 mm × 22 mm. Addressing each speaker with a different phase at a specific time allows periodic excitation. All speakers are calibrated with a microphone placed at $r = 0$ in the actuation plane for all relevant frequency ranges in order to produce repeatable sound pressure levels. Moreover, preliminary hot-wire measurements at no-flow conditions show that the transfer function of input voltage to output peak velocity is linear within the utilized frequency and amplitude ranges. Nonetheless, amplitudes in the lock-in experiments are still given in voltage since the peak velocities at no-flow conditions are likely to be overestimated compared to flow conditions, thus not being directly applicable.

All experiments are conducted for three different mass flows $\dot{m} = 37.5$, 50 and 75 kg/h. These correspond to Reynolds numbers of $\mathrm{Re} = 15,000$, 20,000 and 30,000 based on the bulk velocity $u_0 = \dot{m}/(\rho\pi D^2/4)$ at the tube exit and the tube diameter $D = 51$ mm as the characteristic length, i.e. $\mathrm{Re} = u_0 D/\nu$. The swirl number, based on the axial flux of azimuthal momentum to axial flux of axial momentum [33] is set to $S = 1.18$. This corresponds to vane angles of $\mu = 64.4°$, 63° and 62° for the respective Reynolds numbers. This was verified by preliminary laser doppler velocimetry measurements.

Five actuation positions are tested for the lock-in studies. Measured from the exit plane of the tube these are: $x_a/D = -2$, -1.5, -1, -0.75 and -0.5. Actuation is applied within the range of ±10% of the respective natural frequency. The maximum frequency increments are $\pm 2.5\% f_n$ or lower between the selected forcing frequencies f_f. One of these five actuation positions is exemplarily illustrated in Fig. 3.1. The experimental parameters are summarized in Tab. 3.1.

$\dot{m}$ [kg/h]	u_0 [m/s]	Re [−]	μ [°]	S [−]	x_a/D [−]
37.5	4.3	15,000	64.4	1.18	−2, −1.5, −1, −0.75, −0.5
50	5.7	20,000	63	1.18	
75	8.6	30,000	62	1.18	

Table 3.1: Overview of experimental parameters.

3.1 Measurement Techniques and Data Analysis

All three components of the velocity field are captured by SPIV for the $x_a/D = -2$ configuration. This allows for the characterization of the non-forced flow field in general and the forced flow field for this particular actuator position. A Quantel double-pulse Nd:YAG laser with a wavelength of 532 nm and appropriate optics is used to generate a light sheet of approximately 2 mm thickness. A total number of $N = 1000$ double images per measurement is recorded at a sampling frequency of 5.89 Hz with two PCO CCD cameras in front-scattering configuration, as illustrated in Fig. 3.2. The pulse distances are set according to the respective resulting out-of-plane velocities which differ with the Reynolds number. Flow seeding is achieved with an aerosol of liquid Di-Ethyl-Hexyl-Sebacat. The snapshots with a resolution of 2048 × 2048 pixel are post-processed with a commercial SPIV software. The images are de-warped with the aid of a multi-level

calibration target and a multi-grid cross-correlation scheme with a final window size of 32×32 pixel, a window overlap of 50% and a subpixel peak fit is employed. The resulting velocity field is filtered and outlier values are linearly interpolated from neighboring interrogation windows.

The SPIV domains are separated into an external domain (SPIV domain #1) and an internal domain (SPIV domain #2) and not recorded simultaneously. For #2 the light sheet is introduced from above the tube exit plane. Due to reflections in the actuator plane, the effectively resolved SPIV domain #2 only reaches upstream to $x/D \approx -1.75$. Furthermore, there is an unresolved section between domain #1 and #2 due to the finite thickness of the endplate going from $x/D \approx -0.08$ to 0. For the mean flow, the separated domains are merged by linearly interpolating inside the unresolved section. In case of the POD modes, a similar approach is performed by calculating the modes for each domain separately, then matching their phases and finally linearly interpolating between the modes. Due to the rather large extent of both SPIV domains, the resulting camera resolution is insufficient to accurately capture the boundary layers. The missing velocities very close to the walls are therefore extrapolated from the resolved domains onto a no-slip condition $u = v = w = 0$ on the walls.

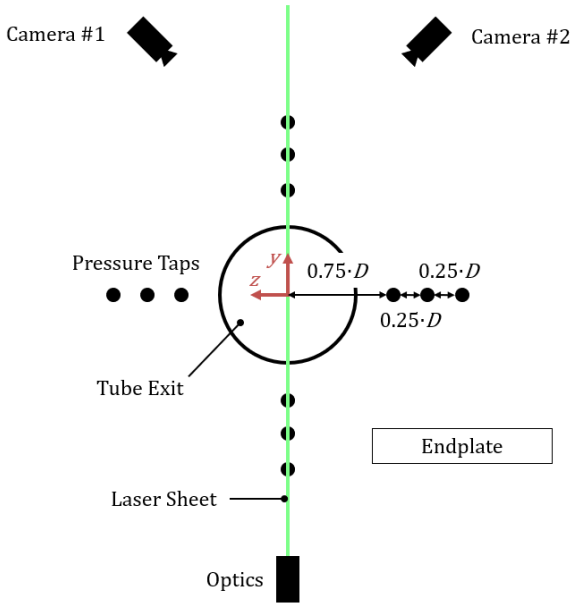

Figure 3.2: Experimental setup, top view, with pressure tap positions, laser sheet and camera arrangement.

The natural frequency of the PVC is extracted via time-resolved pressure signals at a sampling rate of 50 kHz, obtained through pressure taps on the endplate arranged concentrically around the tube exit as displayed in Fig. 3.2. The differential pressure sensors connected to the taps can resolve pressure fluctuations as small as 0.1 Pa. The fluctuating parts of the jth sensors $p_j''(t) = p_j(t) - \overline{p_j}$ are decomposed into spatial Fourier modes with:

$$p_m''(t) = \sum_{j=1}^{4} p_j''(t) \cdot e^{-\mathrm{i}jm \cdot 2\pi/4} \tag{3.1}$$

where $m = 0$, 1 and 2 refer to the azimuthal wave numbers that can be resolved with a total amount of four sensors per circumference. The modes are then transferred into the power spectrum with Welch's method [46] combined with a Hamming windowed sliding average at 50% overlap. For the obtainment of the instantaneous phase angle of the PVC in the lock-in studies, the time signal of azimuthal mode $m = 1$, i.e. $p_1''(t)$, is filtered first with a 20th order Butterworth bandpass filter. The filtered signal is then used to calculate the phase angle via:

$$\varphi_{\mathrm{PVC}}(t) = \arctan\left(\frac{\Im(p_1''(t)|_{\mathrm{filt}})}{\Re(p_1''(t)|_{\mathrm{filt}})}\right). \tag{3.2}$$

3.2 Solving the Linear Stability Analysis

The Fortran code *MAFIA* by Paredes [42] is employed for the discretization and solving of the generalized eigenvalue problem (Eqn. 2.14) with the Arnoldi algorithm. A high-order finite difference scheme with nonuniformly distributed Chebyshev nodes is used for discretization which is able to provide a converged solution at comparatively low mesh resolution.

At the inlet Γ_{in}, homogeneous Dirichlet boundary conditions for velocity and pressure are imposed since the coherent perturbations are assumed to be zero or very close to zero far upstream. This is also cross-checked *a priori* by comparing with the amplitudes of the POD modes at this position. At the axial outlet $\Gamma_{\mathrm{out,x}}$, homogeneous Neumann boundary conditions for the velocity and pressure are set, since the domain is truncated at positions with remaining non-zero perturbations. At the radial outlet $\Gamma_{\mathrm{out,r}}$, asymptotic Dirichlet boundary conditions are set. For all walls Γ_{wall}, homogeneous Dirichlet boundary conditions are imposed for the velocity due to the no-slip and no-penetration condition. For the pressure, no physical boundary conditions exist. However, a compatibility condition from the governing momentum equations can be derived [47]. Substituting the homogeneous Dirichlet conditions from the velocity into the linearized Navier–Stokes equation for coherent perturbation (Eqn. 2.10), knowing that the eddy viscosity is zero per definition on the wall, taking the inner product with the unit normal vector $\mathbf{n}$ at the respective boundaries, and rearranging leads to:

$$\frac{\partial p}{\partial n} = \rho\nu\frac{\partial^2 u_n}{\partial n^2}, \quad \mathbf{x} \in \Gamma_{\mathrm{wall}}. \tag{3.3}$$

Assuming that $\partial^2 u_n/\partial n^2 \approx 0$ provides homogeneous Neumann conditions for the pressure on the walls. Since the global LSA is conducted in a cylindrical coordinate system, the del operator ∇ in Eqn. 2.10 and 2.11 exhibits a singularity in $r = 0$. To ensure smoothness and boundedness on the centerline, the following conditions need to be fulfilled [48]:

$$\lim_{r\to 0}\frac{\partial \widetilde{\mathbf{u}}}{\partial \theta} = 0 \tag{3.4}$$

$$\lim_{r\to 0}\frac{\partial p}{\partial \theta} = 0. \tag{3.5}$$

The left hand side of Eqn. 3.4, without the limit, can be written as:

$$\frac{\partial \widetilde{\mathbf{u}}}{\partial \theta} = \frac{\partial \widetilde{u}}{\partial \theta}\mathbf{e}_x + \widetilde{u}\underbrace{\frac{\partial \mathbf{e}_x}{\partial \theta}}_{=0} + \frac{\partial \widetilde{v}}{\partial \theta}\mathbf{e}_r + \widetilde{v}\underbrace{\frac{\partial \mathbf{e}_r}{\partial \theta}}_{=\mathbf{e}_\theta} + \frac{\partial \widetilde{w}}{\partial \theta}\mathbf{e}_\theta + \widetilde{w}\underbrace{\frac{\partial \mathbf{e}_\theta}{\partial \theta}}_{=-\mathbf{e}_r} \tag{3.6}$$

where ($\mathbf{e}_x$, $\mathbf{e}_r$, $\mathbf{e}_\theta$) is the standard basis of the cylindrical coordinate system. Substituting Eqn. 3.6 in Eqn. 3.4 and, also, substituting the normal mode ansatz of the bi-global LSA from Eqn. 2.13 in Eqn. 3.4 and 3.5 with azimuthal wavenumber $m = 1$, approaching the limit provides the following conditions to hold:

$$\hat{u} = 0, \quad r = 0 \tag{3.7}$$
$$-\hat{w} + \mathrm{i}\hat{v} = 0, \quad r = 0 \tag{3.8}$$
$$\hat{v} + \mathrm{i}\hat{w} = 0, \quad r = 0 \tag{3.9}$$
$$\hat{p} = 0, \quad r = 0. \tag{3.10}$$

Eqn. 3.8 and 3.9 are linearly dependent. To get conditions for $\hat{v}$ and $\hat{w}$ at $r = 0$ the continuity equation from Eqn. 2.11 is considered in cylindrical coordinates on the centerline:

$$\lim_{r\to 0}\left(\frac{\partial \widetilde{u}}{\partial x} + \frac{1}{r}\frac{\partial}{\partial r}(r\widetilde{v}) + \frac{1}{r}\frac{\partial \widetilde{w}}{\partial \theta}\right) = 0. \tag{3.11}$$

It is $\lim_{r\to 0}(\partial\widetilde{u}/\partial x) = 0$ since $\hat{u} = \widetilde{u} = 0$ for $r = 0$ (Eqn. 3.7). Again, the normal mode ansatz from Eqn. 2.13 is substituted which yields:

$$\lim_{r\to 0}\left(\frac{1}{r}(\hat{v} + \mathrm{i}\hat{w}) + \frac{\partial \hat{v}}{\partial r}\right) = 0, \tag{3.12}$$

and approaching the limit with Eqn. 3.9 and L'Hôpital's rule:

$$2\frac{\partial \hat{v}}{\partial r} + \mathrm{i}\frac{\partial \hat{w}}{\partial r} = 0, \quad r = 0. \tag{3.13}$$

From kinematic reasoning, $\hat{v}$ and $\hat{w}$ must be finite on the centerline and, additionally, the radial partial derivative of the radial velocity must vanish, as argued by Batchelor & Gill [49]. Therefore, with regard to Eqn. 3.13, homogeneous Neumann boundary conditions need to be set for $\hat{v}$ and $\hat{w}$ on the axis Γ_{axis}. All boundary conditions are again summarized in Tab. 3.2. For the adjoint modes, the same boundary conditions are applied as for the direct modes, except that the axial inlet and axial outlet conditions from Tab. 3.2 are swapped.

Γ_{in}	$\Gamma_{\text{out,x}}$	$\Gamma_{\text{out,r}}$	Γ_{wall}	Γ_{axis}
$\hat{u} = 0$	$\partial\hat{u}/\partial n = 0$	$\hat{u} = 0$	$\hat{u} = 0$	$\hat{u} = 0$
$\hat{v} = 0$	$\partial\hat{v}/\partial n = 0$	$\hat{v} = 0$	$\hat{v} = 0$	$\partial\hat{v}/\partial r = 0$
$\hat{w} = 0$	$\partial\hat{w}/\partial n = 0$	$\hat{w} = 0$	$\hat{w} = 0$	$\partial\hat{w}/\partial r = 0$
$\hat{p} = 0$	$\partial\hat{p}/\partial n = 0$	$\hat{p} = 0$	$\partial\hat{p}/\partial n = 0$	$\hat{p} = 0$

Table 3.2: Boundary conditions of the global LSA.

Due to the domain truncation at the outlet with non-zero perturbations, radiation boundary conditions would be ideal to avoid spurious reflections of the outgoing waves of the mode. Taking a pragmatic approach, radiation boundary conditions can be approximated by imposing a sponge region that gradually dissipates the waves towards the end of the domain [50]. Here, the last 5% upstream of the end of the domain are sponged. The effective viscosity is artificially, smoothly increased up to a factor of 10 of

its original value which lets the coherent fluctuations gradually decay without adversely affecting the eigenvalue and mode shapes of interest. The smooth transition is achieved with a hyperbolic tangent function. This method has been successfully used in other swirling jets to obtain the global mode [14, 51].

4 Results and Discussion

In this section the results from the non-actuated and actuated (or forced) experiments as well as from the LSA comprising the adjoint modes are presented and discussed.

The power spectral densities (PSD) obtained with the pressure sensors give insight into dominant oscillations. They are shown in Fig. 4.1 for azimuthal modes $m = 0$ to 2 and all three Reynolds numbers. The spectra show a dominant frequency at $f = 60\,\mathrm{Hz}$, 78 Hz and 115 Hz for mode 1 which is the natural frequency f_n of the single-helical PVC mode, respectively. The corresponding Strouhal number $\mathrm{St} = fD/u_0$ is approximately constant being $\mathrm{St} \approx 0.7$. The first harmonic of mode 1 manifests in the double-helical mode 2 at double the natural PVC frequency. The spectra of $m = 0$ show no significant axisymmetric instabilities.

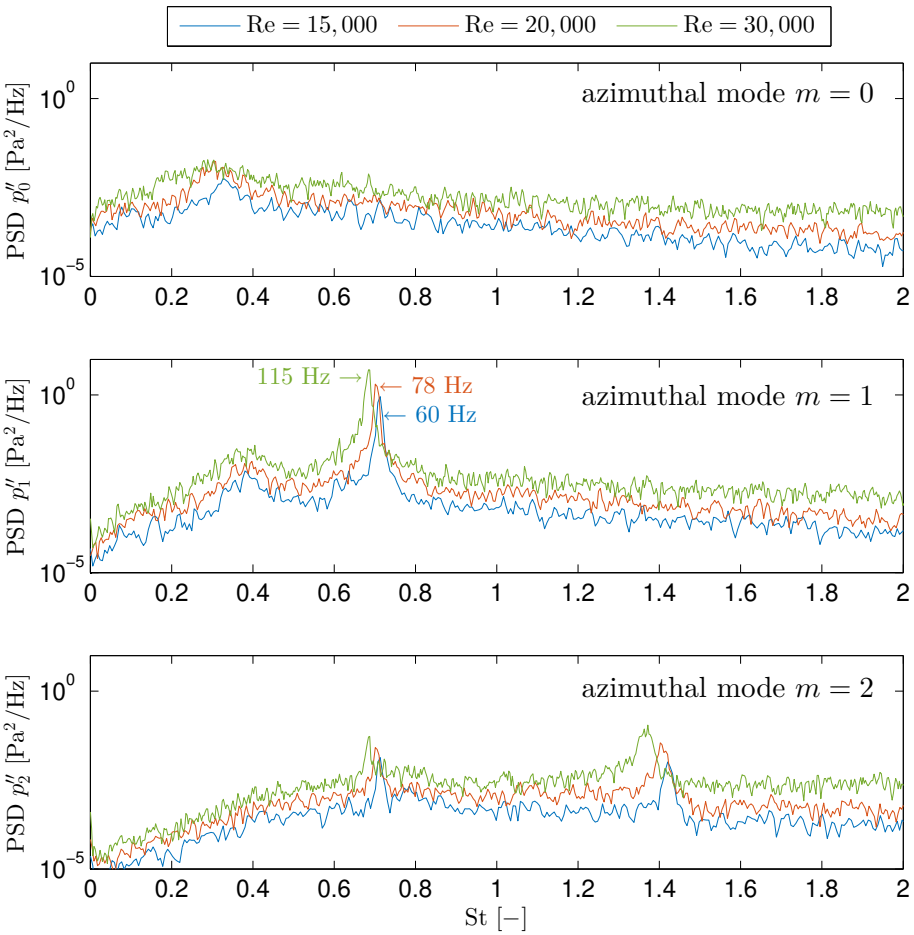

Figure 4.1: Power spectral density over Strouhal number St for azimuthal modes $m = 0$ to 2 and varied Reynolds numbers Re.

4.1 Mean Flow and Coherent Structures

The mean flow and the coherent structures are shortly examined in the following. By choosing the normalization parameters bulk velocity u_0 and mixing section diameter D, the mean flow field can be nondimensionalized. In case of the coherent structures, the normalization is performed with the maximum magnitude of the coherent velocity. Then, the results for all three Reynolds numbers Re = 15,000, 20,000 and 30,000 exhibit a high similarity. Furthermore, the Strouhal number is also nearly the same for all three cases, as stated above. Therefore, for brevity, most of the following discussions can be reduced to considering the results at one Reynolds number only. Here, Re = 20,000 as the intermediate Reynolds number will be picked most of the time.

The normalized mean velocities $(\overline{u}, \overline{v}, \overline{w})$ for Re = 20,000 are displayed in Fig. 4.2. It shows the typical features of a swirling jet with vortex breakdown and an inner and outer shear layer. The prominent recirculation bubble extending from $x/D = 0.18$ to 1.64 is illustrated by the streamlines. The transverse (or radial) velocities closely downstream of the exit clearly show the initial spreading of the swirling jet. The out-of-plane (or azimuthal) velocities show that the swirl is rotating in positive θ-direction.

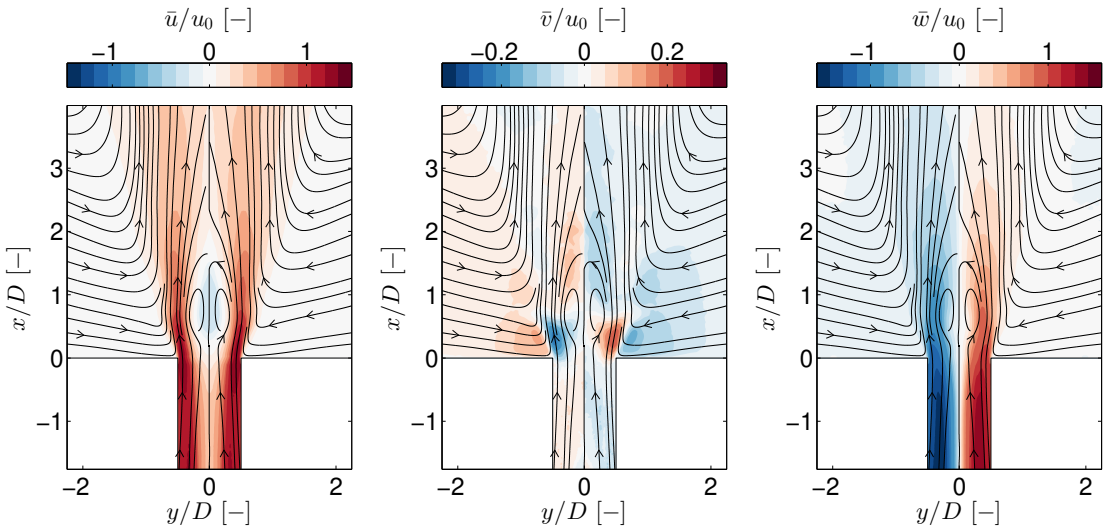

(a) axial **(b)** transverse **(c)** out-of-plane

Figure 4.2: Normalized mean flow, Re = 20,000.

The calculated two most energetic POD modes, superposed according to Eqn. 2.5 at arbitrary phase and normalized on the global maximum magnitude of the three components $|\widetilde{\mathbf{u}}|_{\max}$ are shown in Fig. 4.3a, 4.3b and 4.3c (relative energies of first three POD modes in SPIV domain #1 are $\lambda_1 = 9.5\%$, $\lambda_2 = 8.4\%$, $\lambda_3 = 2.5\%$; in SPIV domain #2 they are $\lambda_1 = 21.3\%$, $\lambda_2 = 17.1\%$, $\lambda_3 = 3.6\%$). The phase portrait of the POD time-coefficients reveals that the two most energetic modes represent an oscillatory, harmonic motion (not shown). Hence, the POD modes represent the coherent fluctuations of the triple decomposition induced by the PVC, oscillating at the frequency of 78 Hz as obtained in the PSD. The modulation of the axial and transverse coherent velocity downstream of the tube exit indicate the helical shear layer vortices due to Kelvin-Helmholtz instabilities with alternating sense of rotation. The out-of-plane and transverse coherent velocities along the centerline describe the precession of the vortex core [12]. It is very interesting to note that the PVC mode extends far upstream of the tube exit, up to $x/D \approx -1.7$

which has not been observed in previous experiments. The global instability mode is therefore not only present in the open jet but also in the wall-bounded flow inside the tube as well.

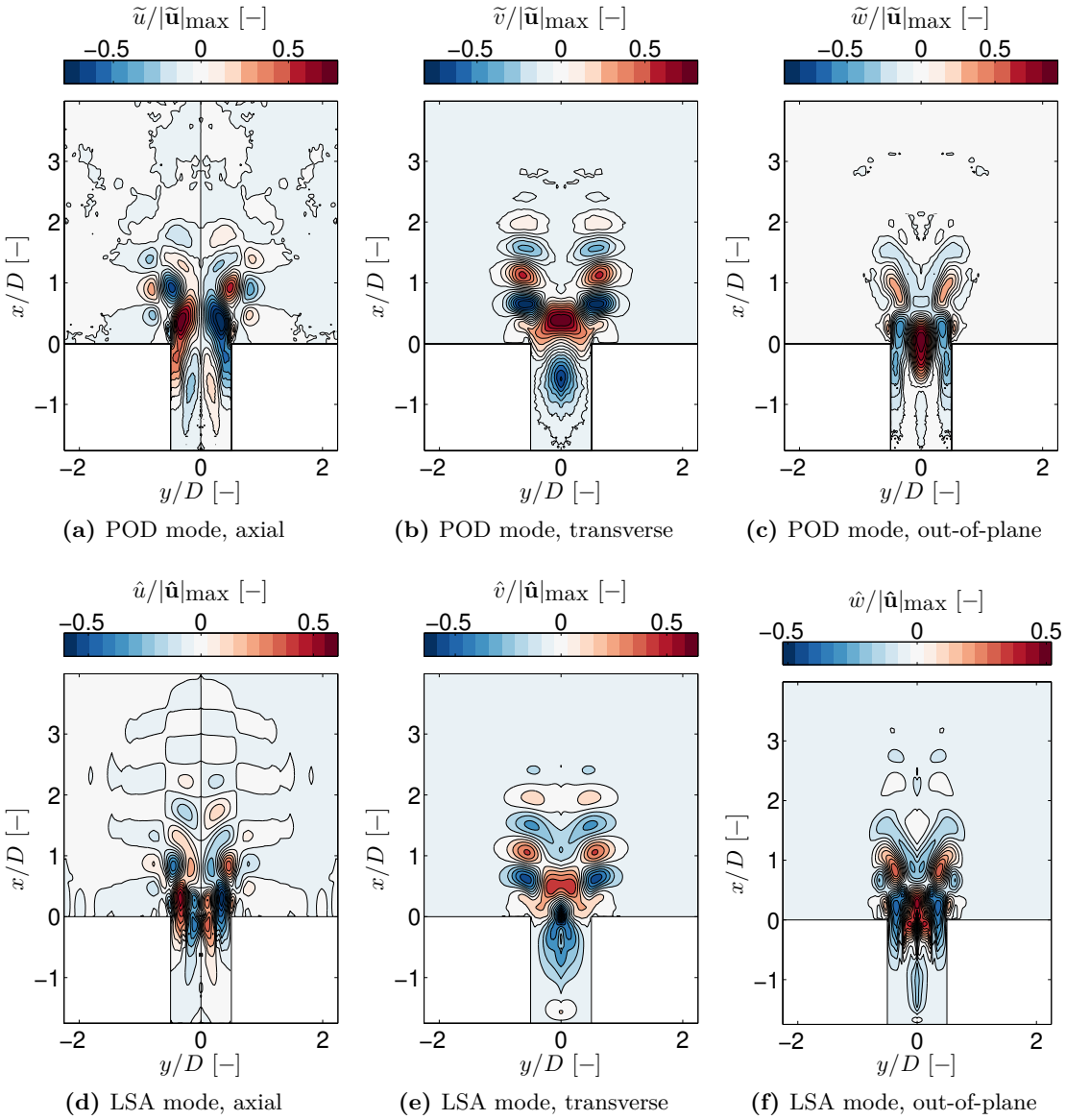

(a) POD mode, axial **(b)** POD mode, transverse **(c)** POD mode, out-of-plane

(d) LSA mode, axial **(e)** LSA mode, transverse **(f)** LSA mode, out-of-plane

Figure 4.3: Normalized POD modes and normalized LSA modes, $\mathrm{Re} = 20,000$.

4.2 Theoretical Prediction of PVC Frequency and Mode

Having obtained the mean flow and POD modes, the mean field is now used for a global LSA to receive a theoretical prediction of the PVC frequency and mode. Figure 4.4 shows the eigenvalue spectra for all three Reynolds numbers. The complex angular frequencies ω are converted to complex frequencies via $f = \omega/(2\pi)$. Then, the real part $\Re(f)$ is a frequency and the imaginary part $\Im(f)$ is a growth rate.

All eigenvalues are stable because they are below the stability limit $\Im(f) = 0$. As stated in Sec. 2.2.2 the PVC at limit cycle is expected to ideally reside exactly on that

limit of $\Im(f) = 0$. The PVC modes are identified to be at $\Re(f) = 62\,\text{Hz}$, 79 Hz and 111 Hz below but close to the stability limit. The real part of the eigenvalue has a maximum uncertainty of ±4% according to a mesh independence study. Within the considered mesh resolutions, the real part converges to a certain value range and starts to oscillate around an average solution. Likewise, the imaginary part oscillates around the stability limit with $\Im(f) = 0 \pm 0.5$. The here displayed cases are the best match cases and the relative errors between predicted and measured natural frequency $f_n = 60\,\text{Hz}$, 78 Hz and 115 Hz are about 3% or less. Also, several modes at smaller frequencies close to the stability limit exist. However, according to the mesh study they are non-physical and of numerical origin since their growth rate tends to decrease with increasing mesh resolution. Their presence does not show any influence on the extracted PVC frequency, growth rate or mode shapes and, thus, can be ignored.

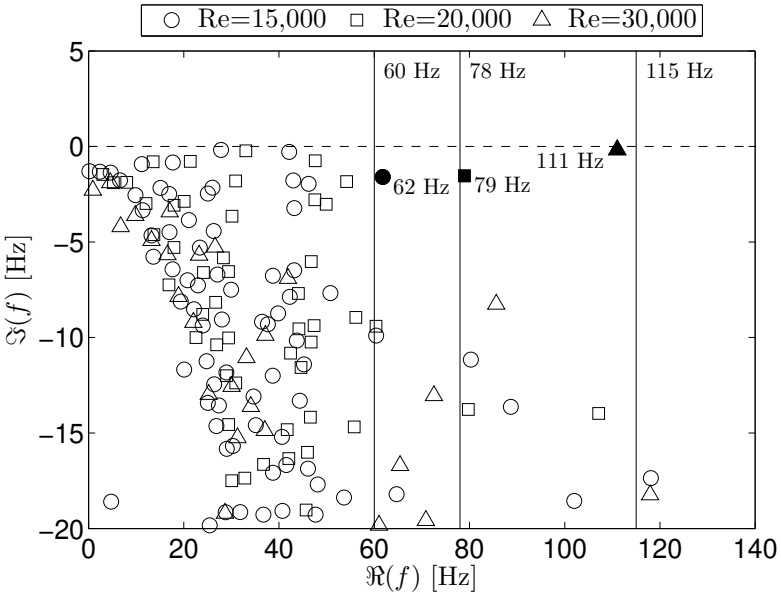

Figure 4.4: Eigenvalue spectrum with frequency $\Re(f)$ and growth rate $\Im(f)$ of the eigenvalues, selected PVC mode (filled markers ●, ■, ▲), measured experimental frequency (vertical solid line) and stability limit (horizontal dashed line).

The real part of the complex amplitude function $(\hat{u}, \hat{v}, \hat{w})$ is displayed in Fig. 4.3d, 4.3e and 4.3f in the case of $\text{Re} = 20,000$. In consistency with the POD mode, the LSA mode is normalized on the global maximum magnitude of the amplitude vector $|\hat{\mathbf{u}}|_{\max}$. The phase is approximately set to match the phase of the POD for comparability. Evidently, the LSA mode shape agrees very well with the POD mode. The dissipation of the modes with increasing downstream location is also well reproduced through the applied eddy viscosity model. A laminar case run with the eddy viscosity set to zero but otherwise same parameters does not exhibit that feature and amplitudes remain high even downstream to the domain end of $x/D = 4$. The excellent agreement between predicted and measured frequency and modes justify the use of the adjoint modes for a theoretical receptivity analysis.

4.3 Theoretical Receptivity Analysis

In the following, the adjoint modes of the PVC are investigated regarding the receptivity of the PVC to open-loop forcing. Figure 4.5 shows the magnitude of each component of the adjoint mode ($|\hat{u}^+|, |\hat{v}^+|, |\hat{w}^+|$) normalized with respect to the global maximum magnitude of the adjoint vector $|\hat{\mathbf{u}}^+|_{\max}$, at $\mathrm{Re} = 20,000$. Again, for both other Reynolds numbers, the adjoint modes are very similar. For the sake of clarity it has to be noted that the contour plots are displayed in cylindrical coordinates this time. The radial coordinate r corresponds to half of the domain with $y \geq 0$. The radial component corresponds to the transverse while the azimuthal component corresponds to the out-of-plane component.

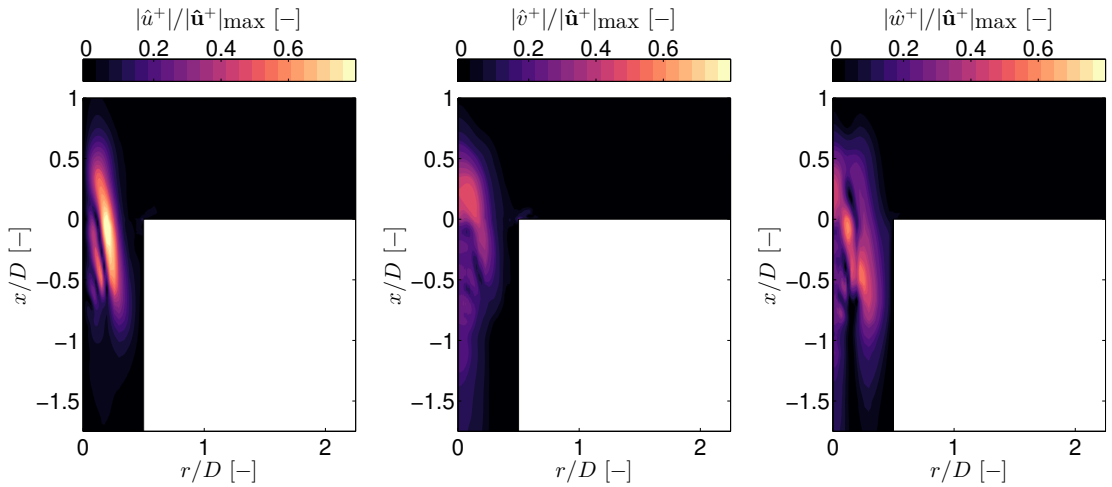

(a) axial **(b)** radial **(c)** azimuthal

Figure 4.5: Normalized magnitude of the adjoint LSA modes, $\mathrm{Re} = 20,000$.

The axial component of the adjoint mode features the highest values compared to the two other components. The regions with high values span a large extent of more than $1 \cdot D$ in axial direction whereas it is localized on a thin strip between centerline and wall in radial direction. The maximum values of the axial component are reached slightly upstream of the tube exit. The receptivity of the PVC to axial forcing is most effective here. The same region for the maximum values is valid for the out-of-plane (or azimuthal) component. For the transverse (or radial) component of the adjoint mode, high values primarily occur around the centerline, with the maximum situated downstream of the exit. Of all components, the radial adjoint exhibits the lowest values. However, together with the azimuthal adjoint it features non-zero values farther upstream of the tube contrary to the axial adjoint. Therefore, when forcing is applied very far upstream the adjoints indicate that the PVC is more receptive to radial and azimuthal actuation. The results affirm the observations of a high receptivity to axial and radial forcing around the exit of the swirling jet reported by Kuhn *et al.* [24] and Lückoff *et al.* [25], when mean flow modifications due to their actuators are disregarded.

The magnitude of the adjoint mode at one fixed point is proportional to the system's response amplitude for a given forcing at this point (see Sec 2.2.3). In previous numerical studies this fact was exploited by implementing a point source of forcing at a specific point to estimate the eigenvalue change of the global mode by structural perturbation theory [17, 51]. However, in this work, the applied actuation cannot be considered as a point source but as a volume source instead. Hence, the implications from the adjoint

modes are less straightforward. Indeed, POD modes of cases with forcing show that the effect of the actuator is spread throughout the entire cross-section. Furthermore, the adjoint is a function of axial and radial coordinates. Thus, for a fixed axial position, assumptions have to be made about what component and what radial position of the adjoint is most relevant for a comparison to the subsequent lock-in studies.

The effect of the actuation is now examined in more detail with the help of an exemplary lock-in case for $\mathrm{Re} = 20,000$, with the actuator at $x_a/D = -2$, $f_f/f_n = 0.95$ and $A_f = 1.3\,\mathrm{V}$. Apart from the region close to the actuator, the POD mode does not change significantly in lock-in state compared to the natural, non-actuated state. By considering only the region inside the tube, it is therefore justified to interpret the locked-in mode $\widetilde{\mathbf{u}}_l$ (reconstructed with POD according to Eqn. 2.5) as a superposition of the natural mode $\widetilde{\mathbf{u}}_n$ and the forcing mode $\widetilde{\mathbf{u}}_f$ as an approximation. The magnitude of the forcing mode is then readily obtained by:

$$|\widetilde{\mathbf{u}}_f| \approx |\widetilde{\mathbf{u}}_l| - |\widetilde{\mathbf{u}}_n| \,. \tag{4.1}$$

The result is shown in Fig. 4.6a, normalized by the global maximum of the magnitude of the vector $|\widetilde{\mathbf{u}}_f|_{\max}$. It has to be emphasized that the actuator is placed at $x_a/D = -2$ in this case. Thus, one does not see the direct impact of the actuation but the impact somewhat downstream. It can be observed that the amplitudes of all three components of the forcing mode are high in the very upstream region and decay quickly towards the tube exit. While the transverse (or radial) component is high along the centerline, the axial component is mainly localized in a region close to the wall. The out-of-plane (or azimuthal) component is high both along the centerline and close to the walls. From these results it is apparent that the PVC is forced in all three directions.

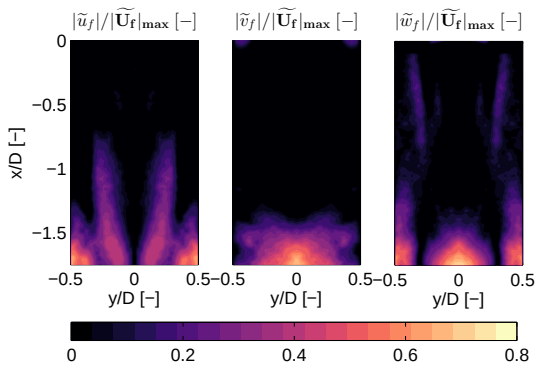

(a) Normalized magnitude of forcing modes (left: axial, center: transverse/radial, right: out-of-plane/azimuthal).

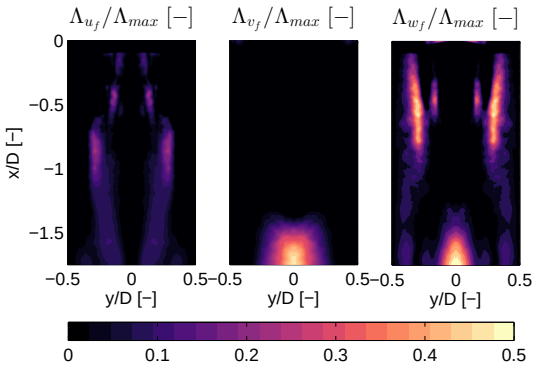

(b) Normalized external feedback for each forcing component (left: axial, center: transverse/radial, right: out-of-plane/azimuthal).

Figure 4.6: Forcing modes and their external feedback in lock-in state inside the tube for $x_a/D = -2$, $f_f/f_n = 0.95$, $\mathrm{Re} = 20,000$.

In order to determine whether the PVC is more receptive to a forcing in one direction than in another and whether their spatial effect can be narrowed down, the feedback (or coupling) of the mode to the external forcing is considered in the following, which

is basically described by the inner product defined in Eqn. 2.39. The magnitude of the numerator can be estimated with the Cauchy–Schwarz inequality:

$$|\langle \hat{\mathbf{u}}^+, \widetilde{\mathbf{u}}_f \rangle| \leq |\hat{\mathbf{u}}^+| \cdot |\widetilde{\mathbf{u}}_f| =: \Lambda. \tag{4.2}$$

The maximum values of Λ reveal the regions of strongest *external* feedback where the coupling of the PVC mode and the forcing mode is the highest. The result of Eqn. 4.2 is shown in Fig. 4.6b for each component separately. The axial component shows low values inside the entire tube. In contrast, the transverse (or radial) as well as the out-of-plane (or azimuthal) component of the external feedback is very high in a localized region around the centerline.

The combined results in Fig. 4.6 show that the forcing is indeed strong in all three components and distributed along the entire cross-section. However, the examination of the external feedback reveals that only the radial and azimuthal component are receptive, and furthermore, that it is very localized along the centerline. It is assumed that a similar localized feedback appears for the other actuator positions. This leads to the hypothesis that, at a fixed axial location, the effect of the forcing is primarily dictated by the magnitude of the radial and azimuthal adjoint mode on the centerline. The theoretical receptivity χ_t is thereby defined as:

$$\chi_t = |\hat{v}^+|_{r=0} \quad \text{and} \quad |\hat{w}^+|_{r=0}\,. \tag{4.3}$$

Figure 4.9 shows these values for the four actuator positions $x_a/D = -1.5$ to -0.5 for all Reynolds numbers. It can be seen that the theoretical receptivity is low in the upstream region of the tube and increases downstream until to the position of $x_a/D = -0.75$ where it reaches a local maximum. Thereafter, it decreases. The receptivity to radial and azimuthal forcing is equal and therefore shown as one line. For $\mathrm{Re} = 15,000$, the most upstream receptivity goes against the trend of both other Reynolds numbers.

4.4 Experimental Receptivity Analysis

In this section, the results of the lock-in experiments are discussed and then compared to the results of the adjoints to validate the theoretically obtained receptivity.

The results of all lock-in cases at $\mathrm{Re} = 20,000$ are illustrated in Fig. 4.7, showing the lock-in amplitude A_l required for PVC lock-in over the forcing frequency f_f normalized with the natural frequency f_n. The precision with which these lock-in amplitudes are determined is limited to $\pm 0.05\,\mathrm{V}$. Two general trends can be made out: The minimum required forcing amplitude increases when the difference between forcing frequency and natural frequency $|f_f - f_n|$ increases. Following the actuator positions from $x_a/D = -2$ downstream an inverse trend can be made out: moving the actuator closer to the tube exit the lock-in amplitude decreases until to the position of $x_a/D = -0.75$. On the upper branch ($f_f > f_n$) this trend continues downstream to $x_a/D = -0.5$, although the change is marginal. However, for the lower branch ($f_f < f_n$) the lock-in amplitude slightly increases again.

For all actuator positions the lock-in amplitudes increase almost linearly with increasing distance between the forcing frequency and the natural frequency. This can be well observed considering the linear fits of the measured lock-in amplitudes. The lock-in curves for $x_a/D = -1$ to -0.5 are approximately symmetrical to $f_f/f_n = 1$ with a slight tendency towards higher lock-in amplitudes for higher frequencies. However, for the actuator positions $x_a/D = -2$ and -1.5, this symmetry does not apply. For $f_f > f_n$,

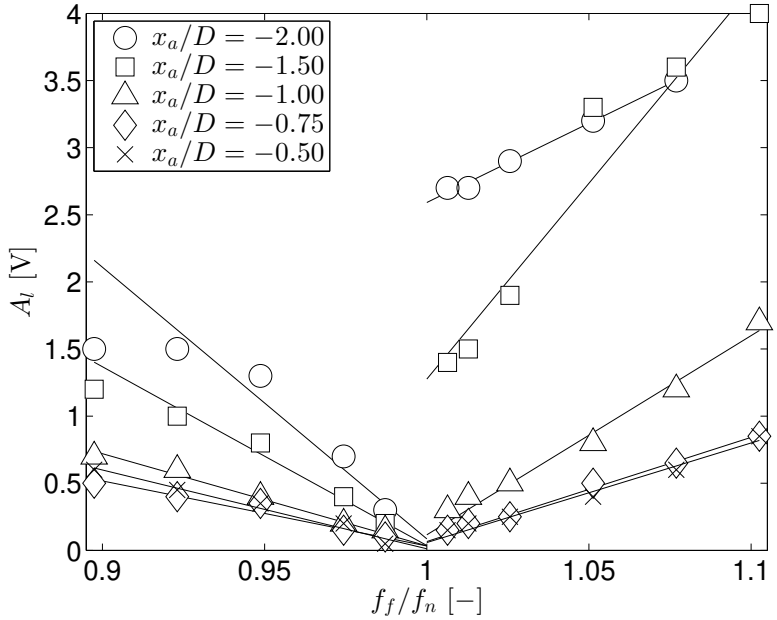

Figure 4.7: Lock-in diagram with linear fits for varied actuator positions x_a/D, Re = 20, 000.

a threshold of the forcing amplitude has to be exceeded before any lock-in occurs even at forcing frequencies very close to the natural one. Apart from this strong asymmetry, the lock-in results reflect the typical behavior of a synchronized self-excited oscillator, as discussed in Sec. 2.1.3.

All of these observed trends for Re = 20, 000 are very similar for the other two Reynolds numbers, except that the lock-in amplitudes are lower for Re = 15, 000 and higher for Re = 30, 000. This results from the corresponding momentum which is required to be introduced for lock-in, when the mean momentum of the flow is lower or higher. Thus, it is not surprising that the lock-in amplitudes scale well with the square of the bulk velocity, i.e. $A_l \propto u_0^2$. Figure 4.8 shows the lock-in amplitudes normalized by the square of the bulk velocity for all three Reynolds numbers. Each of the lock-in branches collapse well on each other.

In the following, a link to the theoretical receptivity discussed in Sec. 4.3 is made. As argued in Sec. 2.2.3 the magnitude of the adjoint mode is proportional to the change of the eigenmode frequency when an arbitrary but fixed forcing is applied. This can also be interpreted as a gradient of the frequency due to a given lock-in amplitude, i.e. $\Delta f/\Delta A_l$. As mentioned above, a trend of a decreasing lock-in amplitude from $x_a/D = -2$ to -0.75 for $f_f < f_n$ was stated which corresponds to a decreasing linear slope $\Delta A_f/\Delta f$. For $x_a/D = -0.5$ it was noted that the lock-in amplitude increases again which corresponds to an increasing linear slope. For $f_f > f_n$ the linear slope decreased monotonously from $x_a = -2$ to -0.5. These statements are visualized in Fig. 4.9 where the *inverted* magnitude of the linear slopes are given downstream of $x_a/D = -1.5$, hereby defining the experimental receptivity χ_e as:

$$\chi_e = \frac{|\Delta f/f_n|}{\Delta A_l} \,. \tag{4.4}$$

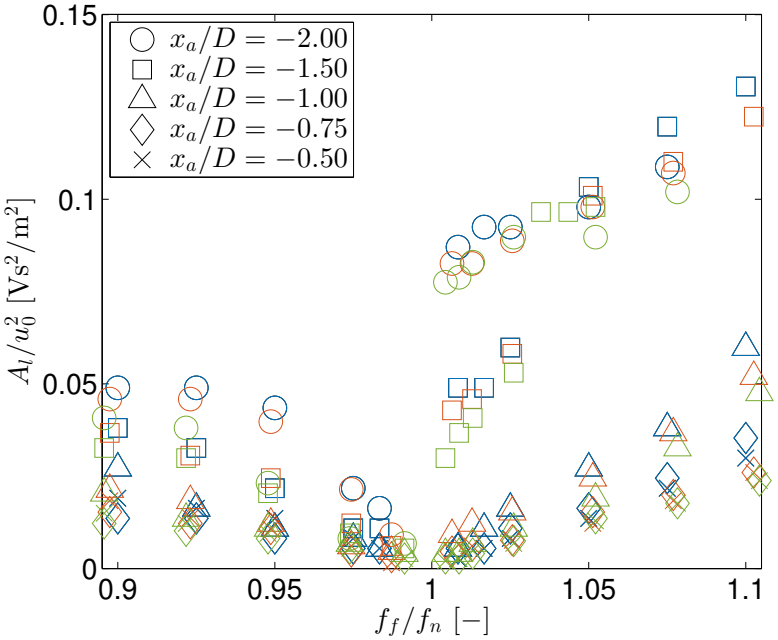

Figure 4.8: Lock-in diagram with normalized lock-in amplitude A_l/u_0^2 for varied actuator positions x_a/D and for all Reynolds numbers (blue: Re = 15,000, red: Re = 20,000, green: Re = 30,000).

The inverted linear slope corresponds to a normalized 'frequency-change gradient'—i.e. how strong is the change of frequency for an arbitrary but fixed forcing amplitude. For below-natural forcing, the dash-dot line shows that the experimental receptivity increases until $x_a/D = -0.75$ and then decreases for $x_a/D = -0.5$. For above-natural forcing, the dashed line shows a continuous increase of the experimental receptivity. Furthermore, the experimental receptivity is higher for forcing frequencies below natural frequency and lower for forcing frequencies above natural frequency. Evidently, the system is more receptive to a decrease of its natural frequency than to an increase.

Comparing the results for $f_f < f_n$ of the experimental receptivity with the theoretical receptivity, it is obvious that the trend of the slowly increasing experimental receptivity from $x_a/D = -1.5$ to the maximum value at -0.75 is well reproduced by the theoretical receptivity, except for Re = 15,000. Farther downstream at $x_a/D = -0.5$, the theoretical receptivity decreases in the same way as the experimental. It has to be emphasized that the maximum receptivity at $x/D = -0.75$ refers to a *local* maximum within the considered region between $x/D = -1.5$ and -0.5 and must not be confused with the *global* maximum receptivity situated farther downstream as seen in Fig. 4.5. The trends of the theoretical receptivity are more in line with the experimental receptivity for below-natural forcing. This asymmetrical behavior could be a hint that the physical mechanism of lock-in for above-natural forcing is slightly different to what could be predicted by the adjoint modes, especially in case of the two upstream positions $x_a/D = -2$ and -1.5. Nonetheless, the theoretical receptivity provides a sufficient estimate for the experimental receptivity.

4.5 Path to Lock-In

The actual lock-in path of the PVC has been ignored so far. Furthermore, recalling the lock-in diagram in Fig. 4.7, the upper branches ($f_f > f_n$) at the two most upstream

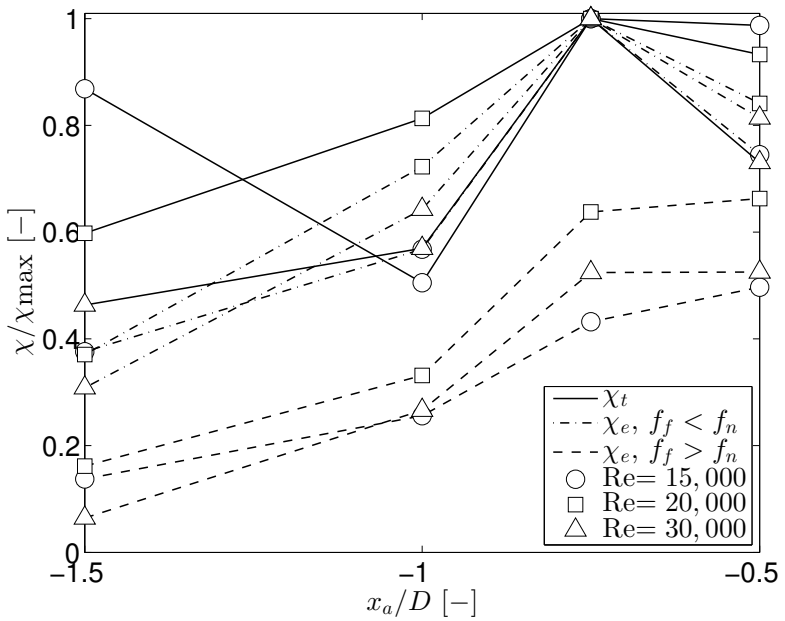

Figure 4.9: Normalized theoretical receptivity $\chi_t/\chi_{t,\max}$ and experimental receptivity $\chi_e/\chi_{e,\max}$ for varied actuator positions x_a/D and Reynolds numbers Re.

actuator positions ($x_a/D = -2$ and -1.5) show a completely different behavior compared to all other cases. To bring clarification, the dynamical behavior is investigated in the following and, along the way, compared to the dynamics of the VDP oscillator from Sec. 2.1.3.

Figure 4.10 shows the lock-in route for selected cases at Re = 30,000. In (a), the natural state of the PVC is displayed, based on the bandpass-filtered signal according to Sec. 3.1. Similar to Fig. 2.3 of the VDP oscillator, the limit cycle is represented by the circular orbits in the phase space (a,i). However, due to the noisy, turbulent conditions, the amplitude of the PVC is not constant over time which becomes clear in the Poincaré map (a,ii). The periodicity is not represented by a fixed point anymore. Therefore, in the power spectrum, the spectral peak at the natural frequency is rather broad compared to the VDP oscillator (a,iv).

When forcing is applied at $x_a/D = -2$, $f_f/f_n = 0.95$ below natural frequency and $A_f = 1\,\mathrm{V}$ below lock-in amplitude, a torus appears in the phase space due to quasiperiodicity (b,i). Correspondingly, the Poincaré map shows numerous possible states for every periodic recurrence of the system to the Poincaré section since the PVC and the forcing oscillations are not phase-related. This is also verified by the phase angle difference $\Delta\varphi$ which increases over time (b,iii). The PSD reveals that the PVC amplitude is only slightly diminished and that the PVC frequency is shifted away from its natural frequency f_n towards the forcing frequency f_f (b,iv), which is known as frequency pulling [38]. Thus, the lock-in route for this particular case may be attributed to the phase lock mechanism. When the forcing amplitude $A_f = 1.9\,\mathrm{V}$ exceeds the lock-in amplitude, the torus vanishes and a new circular orbit emerges (c,i). Hence, the PVC oscillates in phase with the forcing (c,iii). The Poincaré map shows that the system indeed returns to approximately the same state after each cycle (c,ii). After each period a similar forcing amplitude with a corresponding similar PVC amplitude is reached. However, a single fixed point such as for the VDP oscillator does not exist due to the presence of turbulent noise. The PSD now indicates only one dominant peak at the forcing frequency (c,iv).

When forcing is applied at the same actuator position ($x_a/D = -2$), but $f_f/f_n = 1.03$ above the natural frequency and at $A_f = 5\,\mathrm{V}$ prior to lock-in, again a torus can be observed in the phase space (d,i). Likewise, the quasiperiodic behavior is demonstrated in the Poincaré map since recurrence is not coupled to a specific forcing amplitude (d,ii). Accordingly, the phase angle difference grows in magnitude (d,iii). The sign of the phase angle difference is now negative per definition because the forcing oscillates faster than the PVC. Looking at the PSD, it is evident that the PVC amplitude is greatly reduced compared to its natural state. The residual peak of the PVC at $f_f/f_n \approx 0.96$ is also shifted away from both the natural and the forcing frequency (d,iv), which could be denominated as frequency pushing. This observation suggests that the lock-in route which is taken for this case is related to the suppression mechanism. Increasing the forcing amplitude $A_f = 6.6\,\mathrm{V}$ to reach lock-in, circular orbits appear in the phase space, as expected (e,i). From the Poincaré map it is difficult to judge whether lock-in has been reached (e,ii), however the phase angle difference clearly proves that this is the case (e,iii). In the PSD plot the residual peak has vanished and one dominant peak resides at the forcing frequency (e,iv).

When forcing is applied at the actuator position $x_a/D = -0.75$ where the anomalous behavior along the upper lock-in branch does not occur, the lock-in route is qualitatively different. At $f_f/f_n = 1.05$ above the natural frequency and at $A_f = 0.6\,\mathrm{V}$ prior to lock-in, the system's behavior (f) is much more in line with (b). The PVC frequency is pulled away from the natural frequency towards the forcing frequency (f,iv). When lock-in is reached at $A_f = 1\,\mathrm{V}$, the PVC oscillates in phase with the forcing (g,iii) and the Poincaré map clearly shows that the system periodically returns to the same state (g,ii).

These observations indicate that the lock-in branches from Fig. 4.7, where the lock-in amplitude does not go to zero when the forcing frequency approaches the natural frequency (i.e. for $x_a/D = -2$ and -1.5 with $f_f > f_n$), can be interpreted as the suppression lock-in route. The instantaneous PVC frequency is pushed away from the natural and forcing frequency while its amplitude is reduced with increasing forcing amplitude. In other words, the natural dynamics have to be suppressed up to a certain degree whereupon the forcing dynamics are imposed on the system which 'overwrite' the natural behavior. All other cases may be interpreted to follow the phase lock route where the natural dynamics are only manipulated but not completely suppressed such that the PVC consequently 'obeys' the 'clockwork' of the forcing [36]. It has to be emphasized that a reduction of the PVC amplitude also occurs when the ostensible phase lock route is taken. This may be attributed to a spatial shift of the PVC away from the pressure sensors at $x/D = 0$. It could also be a hint that the lock-in actually occurs due to both mechanisms, phase lock *and* suppression. Which of the mechanisms predominates depends on the specific case.

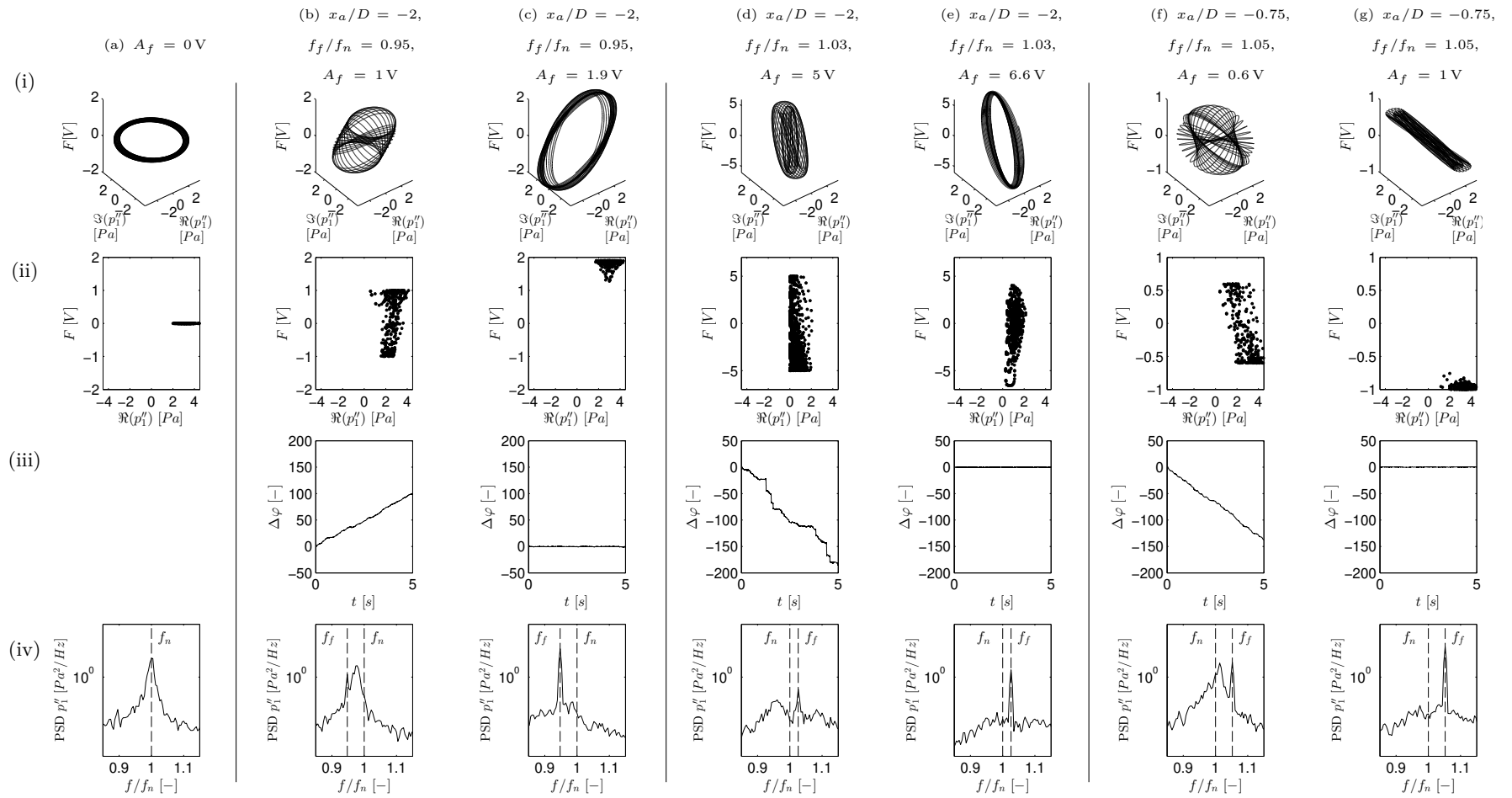

Figure 4.10: Lock-in route of the PVC for selected cases, Re = 30,000, (i) phase space: forcing oscillation F over PVC oscillation p_1'', (ii) Poincaré map: forcing oscillation F over real part of PVC oscillation $\Re(p_1'')$ with $\Im(p_1'') = 0$, (iii) phase angle difference $\Delta\varphi$ over time t, (iv) power spectral density of p_1'' over normalized frequency f/f_n.

4.6 Mean and Coherent Flow Modifications at Lock-In

The changes to the mean and coherent flow field at lock-in, caused by the forcing, are discussed in this section. This discussion is limited to the cases with actuator position $x_a/D = -2$ since SPIV was conducted for these only.

Examining the mean flow fields of different lock-in cases reveals non-negligible mean flow changes. One remarkable change can be observed in the azimuthal velocity which can be characterized by the mass-specific total mean kinetic energy (KE) of the azimuthal velocity at a cross-section of a given axial coordinate x which can be calculated by:

$$\overline{K}_w(x) = \frac{1}{2} \int_0^{2\pi} \int_0^{\infty} \overline{w}^2 r \mathrm{d}r \mathrm{d}\theta. \tag{4.5}$$

Figure 4.11 shows the total mean azimuthal KE per cross-section for $x_a/D = -2$ at $\mathrm{Re} = 15,000$, normalized on the most upstream value of the non-forced case. For readability, only every 5th marker is plotted. The total mean azimuthal KE is reduced at lock-in in comparison to the non-forced case, for both low and high forcing frequencies. At below-natural forcing, the KE decreases with decreasing frequency, particularly upstream of the tube exit ($x/D < 0$). At above-natural forcing, the KE is even more diminished. These observed trends also apply when the total mean KE of all three components is considered (not shown). Hence, there is a significant net effect of the forcing onto the mean flow. The forcing causes a dissipation of the mean KE which decreases the rotation rate of the swirling jet. This dissipation is likely caused by additional small-scale turbulence resulting from the ZNMF jets introduced by the actuator.

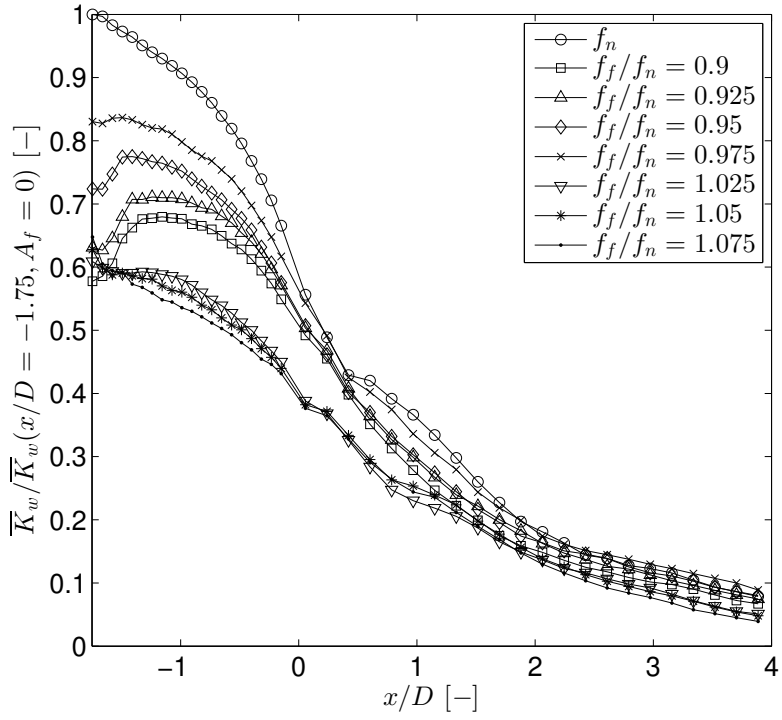

Figure 4.11: Total mean azimuthal kinetic energy $\overline{K}_w$ as a function of axial coordinate x/D for natural and locked-in PVC, actuator position $x_a/D = -2$, $\mathrm{Re} = 15,000$.

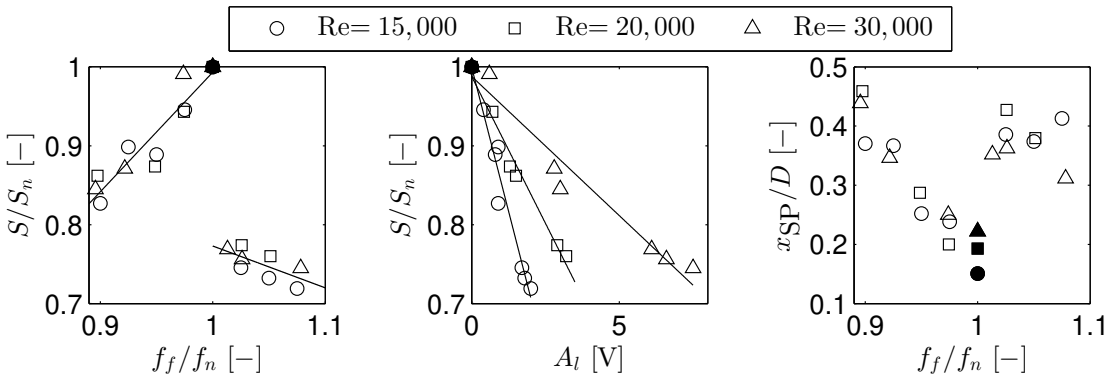

Figure 4.12: Swirl number and stagnation point modifications for locked-in PVC, actuator position $x_a/D = -2$ (left: normalized swirl number S/S_n over normalized forcing frequency f_f/f_n, center: normalized swirl number S/S_n over lock-in amplitude A_l, right: axial stagnation point location x_{SP}/D over normalized forcing frequency f_f/f_n; filled markers ●, ■, ▲: non-forced, natural case, solid line: linear fit).

Corresponding to the reduction of the azimuthal velocities, the swirl number decreases as well. In the left-hand plot of Fig. 4.12 the swirl number S, normalized with the natural swirl number of the non-forced PVC, S_n, is displayed as a function of the normalized forcing frequency f_f/f_n. When the PVC is locked-in at below-natural forcing, the swirl number continuously decreases with approximately linear proportion when the forcing frequency is lowered. For above-natural forcing, the swirl number is discontinuously reduced compared to the natural case, analog to the discontinuous lock-in behavior. In the center plot of Fig. 4.12, it becomes evident that the normalized swirl number is actually a function of the lock-in amplitude A_l. For each respective Reynolds number, the swirl number decreases linearly with increasing lock-in amplitude. Therefore, a significant impact of the forcing is the reduction of the swirl number. Likewise, this swirl number reduction is reflected by the downstream shift of the stagnation point of the breakdown bubble, as shown in the right-hand plot of Fig. 4.12. For below-natural forcing, the stagnation point is shifted in linear proportion to the decrease of the forcing frequency. This correlation of downstream shift and swirl number decrease is also a typical feature for non-forced PVC [33]. However, at above-natural forcing, there is no definite trend. Additionally, compared to below-natural forcing, the stagnation point is not shifted farther downstream although the swirl number is much lower.

It is reasonable to expect that these mean flow modifications have a significant influence on the PVC and that the underlying lock-in mechanisms are related to them. Deeper insight can be gained by conducting a global LSA of the locked-in mean flows. In the left-hand plot of Fig. 4.13 the PVC frequency obtained from the LSA is shown as function of the experimentally obtained PVC frequency at lock-in. Provided that the lock-in is only caused by a mean flow modification, the PVC frequency from the LSA would ideally match the experimental PVC frequency. This line of identity is displayed as a dash-dot line. The predicted LSA frequencies are closely gathered around that line for below-natural forcing. Therefore, for these cases it can be stated that lock-in is primarily caused by a mean flow modification. The frequency of the PVC is lowered by a net reduction of the swirl number.

In contrast, the LSA results for above-natural forcing clearly suggest that lock-in is not reached by a mean flow modification. Although the experimental PVC frequency is above the natural frequency, the LSA predicts frequencies below. Since the LSA frequency

is coupled to the mean flow, it is not surprising that the LSA frequency deviates more and more from the natural frequency when the modifications to the mean flow become greater, i.e. when the lock-in amplitude increases, as shown in the center plot of Fig. 4.13. A linear relation can be made out for each Reynolds number. The qualitative similarity to the left-hand and center plot of Fig. 4.12 strongly suggests that the LSA frequency can be directly described as a function of the swirl number. This is displayed in the right-hand plot of Fig. 4.13. The LSA frequency has an approximately linear relation with regard to the swirl number. Thus, the predicted frequency of the mean flow is determined by the swirl number. Since the actual PVC frequency in the experiment is larger than the natural frequency for $f_f > f_n$, but the mean flow state predicates that the PVC frequency is supposed to be lower than natural, the lock-in for above-natural forcing at $x_a/D = -2$ clearly cannot be described by mean flow modifications and lock-in is reached through a different mechanism.

The growth rates of all LSA cases do not reveal any clear trend (not shown). This is likely to be related to the oscillating converged solution for even high mesh resolutions, as mentioned in Sec. 4.2. The solution oscillates around the stability limit $\Im(f) = 0$ which renders definite conclusions about the stabilizing or destabilizing effect of the forcing onto the mean flow difficult. For now, it can only be concluded that the growth rate is not significantly changed by the forcing.

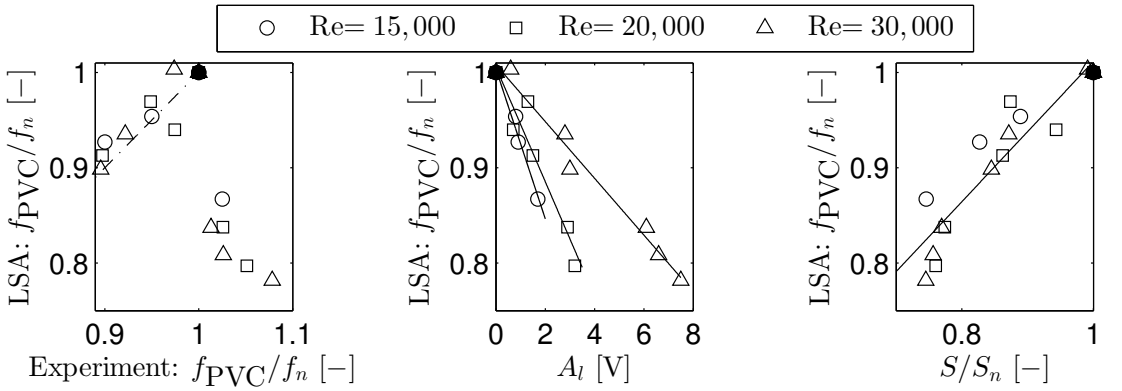

Figure 4.13: PVC frequency predicted by global LSA due to mean flow modifications at lock-in, actuator position $x_a/D = -2$ (left: normalized PVC frequency f_{PVC}/f_n of LSA over normalized PVC frequency of experiment, center: normalized PVC frequency f_{PVC}/f_n of LSA over lock-in amplitude A_l, right: normalized PVC frequency f_{PVC}/f_n of LSA over normalized swirl number S/S_n; filled markers ●, ■, ▲: non-forced, natural case, solid line: linear fit, dot-dash line: line of identity where LSA PVC frequency equals experimental PVC frequency).

The lock-in path for $x_a/D = -2$, as discussed in Sec. 4.5, can now be interpreted in a more phenomenological way. On the phase lock route for below-natural forcing, frequency pulling occurred prior to lock-in, i.e. the PVC frequency was shifted from the higher natural frequency towards the lower forcing frequency. This may be seen as an intermediate state where the swirl number has not yet been sufficiently reduced such that the PVC frequency does not yet match the forcing frequency. For above-natural forcing, the suppression route was accompanied by frequency pushing, i.e. the PVC frequency was lowered and shifted away from both the higher natural frequency and forcing frequency. Again, this may be explained by the reduction of the swirl number due to the forcing.

For actuator positions $x_a/D \geq -1$, where the lock-in branches are *almost* symmetrical to $f_f = f_n$, no SPIV data was recorded. It would be interesting to know whether for above-natural forcing the mean azimuthal KE actually increases, leading to a higher rotation rate of the swirling jet and a higher swirl number. By this mean flow modification, the PVC frequency would be increased then. However, this would require a net energy flux from the turbulent flow to the mean flow [52]. An argument in favor of this theory can be made out from the observations in Sec. 4.5. For $x_a/D = -0.75$, frequency pulling also occurs for above-natural forcing which could be interpreted as an increase of the swirl number due to a mean flow modification. Furthermore, for $x_a/D = -2$, the mean azimuthal KE appears to recover and increase again downstream of the actuator, as seen in Fig. 4.11. This shows that a net energy flux from the turbulent field to the mean field in this setup can occur.

On the other hand, the swirl number being a linear function of the lock-in amplitude strongly suggests that the effect of the forcing is always a reduction of the rotation rate and thus the swirl number, even for the actuator positions $x_a/D \geq -1$. This in turn may also provide a heuristic argument why the lock-in amplitude is larger for $f_f > f_n$: The forcing adversely modifies the mean flow that would cause the PVC frequency to decrease due to a lowered swirl number. Additional energy input, provided by the actuation, is required in order to pull the frequency of the PVC back to the higher forcing frequency. This results in the experimental receptivity being lower for $f_f > f_n$ compared to the experimental receptivity being higher for $f_f < f_n$.

No statements have been made yet whether the PVC mode significantly changes due to the forcing. Similar to Eqn. 4.5, the total coherent KE of the PVC is used to characterize its changes caused by the forcing. It is calculated by:

$$\widetilde{K}(x) = \frac{1}{2} \int_0^{2\pi} \int_0^{\infty} |\widetilde{\mathbf{u}}|^2 r \mathrm{d}r \mathrm{d}\theta. \tag{4.6}$$

At the most upstream position $x/D = -1.75$, Fig. 4.14 shows that in the non-forced case the coherent KE is zero at this location. When forced, the introduced perturbations increase the total coherent KE with larger distance of forcing frequency to natural frequency due to the larger amplitudes of the ZNMF jets. However, in all cases they decay downstream. Hence, there are no convective instabilities which are amplified at this most upstream location. For below-natural forcing, at $x/D \approx -1$ the coherent KE has approximately decayed down to the same level as for the non-forced case. It is interesting to note that the position of this trend reversal from decay to growth correlates well with the saturation of the mean azimuthal KE that grows until $x/D \approx -1$ and decays downstream. This observation is a strong indicator that there must be an energy flux from the coherent field to the mean field.

Downstream from $x/D \approx -1$, the changes in the axial energy distribution are marginal for all cases where $f_f < f_n$. This has already been implicitly verified in Sec. 4.3 in order to derive an approximation of the forcing mode. The coherent structures are spatially amplified downstream and saturation is reached between $x/D \approx 0.4$ to 0.6, depending on the respective forcing frequency. In general, the below-natural locked-in PVC exhibits higher saturation amplitudes than the natural PVC. From $f_f/f_n = 0.975$ to $f_f/f_n = 0.925$ the saturation amplitude increases corresponding to the increased forcing amplitude. However, for $f_f/f_n = 0.9$ the trend is reversed and the saturation amplitude decreases. In any case, the forcing has a non-vanishing effect that slightly amplifies the PVC amplitudes. Since the growth rate of the PVC based on LSA showed no significant changes, it can

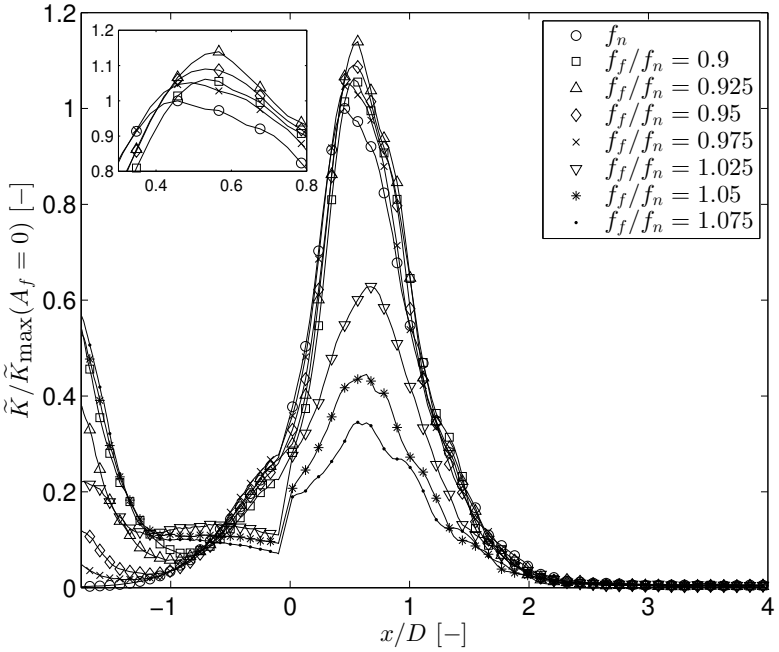

Figure 4.14: Total coherent kinetic energy $\widetilde{K}$ as a function of axial coordinate x/D for natural and locked-in PVC, actuator position $x_a/D = -2$, Re $= 15,000$ (inset: detail of energy saturation region).

be hypothesized that the growth of the PVC amplitude is caused by a nonlinear mode interaction between forcing mode and PVC mode. Thus, the effect of the forcing is not only to change the mean flow, although this effect predominates. This seemingly minor detail may be very important for the the cases with above-natural forcing for $x_a/D \geq -1$. Here, one hypothesis was that at these actuator positions the swirl number is also reduced by the forcing, leading to a PVC frequency reduction, when the mean field alone is considered. Hence, in order to still increase the PVC frequency towards the forcing frequency, the introduced perturbations need to be sufficiently large such that they overwhelm the perturbations of the PVC by a nonlinear mechanism. After all, it appears that lock-in cannot be fully described by mean flow modifications only.

For above-natural forcing, the saturation amplitude is greatly diminished compared to the non-forced case. With increasing forcing frequency, the saturation amplitude decreases. This is probably related to the suppressing character that effectively reduces the swirl number, as mentioned above. Lock-in can then be explained by the requirement that the introduced perturbations need to be sufficiently strong in amplitude such that their decay downstream is not critical. Then, these perturbations have a non-negligible influence on the dynamics of the PVC when the region of absolute instability downstream of the tube exit is reached where the forcing and the PVC couple nonlinearly.

In the end, the simplifying assumption that the mean flow does not change turns out to be unjustified. The changes in the mean flow are to such an extent that the global LSA of the locked-in fields provide different results than the global LSA of the non-forced, natural field. In fact, the global LSA is able to predict the locked-in PVC frequency with satisfying accuracy.

In Sec. 2.2.3 the adjoint mode was motivated by introducing an open-loop source term to the linearized Navier–Stokes equation for the coherent fluctuation (Eqn. 2.23) under the aforesaid assumption that the mean flow is not modified by the forcing. On

the one hand, the assumption does not hold true. But on the other hand, the adjoint analysis still provides an acceptable estimation for the PVC's receptivity. The question, why this is the case, can be answered by the structural perturbation theory. Within that theory, the adjoint modes can be used to give an exact first-order change of the eigenvalue when the operator defining the eigenvalue problem is perturbed. The forcing is then not mathematically modeled to act as a momentum source anymore, yielding an inhomogeneous partial differential equation (Eqn. 2.23). Instead, the forcing is modeled to act as a perturbator of the original homogeneous partial differential equation (Eqn. 2.12)—i.e. the structure of the problem is perturbed. The first-order change of an eigenvalue ω_j can then be calculated by [43]:

$$\mathrm{d}\omega_j = \frac{\langle \hat{\mathbf{q}}_j^+, \mathrm{d}\mathbf{A}\hat{\mathbf{q}}_j \rangle}{\langle \hat{\mathbf{q}}_j^+, \mathbf{B}\hat{\mathbf{q}}_j \rangle}. \tag{4.7}$$

Note the similarity to Eqn. 2.39 which defined the receptivity of the PVC due to an open-loop forcing for an unmodified mean flow. Now, the change of the eigenvalue is proportional to the magnitude of the adjoint mode $\hat{\mathbf{q}}_j^+$ as well as the magnitude of the direct mode $\hat{\mathbf{q}}_j$ and the change of the discretized operator $\mathbf{A}$. In $\mathbf{A}$ the mean flow field is contained. For a given natural state of the PVC, the adjoint and direct mode are fixed. It then follows that $|\mathrm{d}\omega_j| \propto |\mathrm{d}\mathbf{A}|$. The structural perturbation needs to be larger in magnitude when the forcing frequency is further away from the natural frequency. This, again, is in accordance with the observations of the experimental lock-in studies: For increased distance of the forcing frequency to the natural frequency, the forcing amplitude needs to be increased which results in an increase of the mean flow modifications. Furthermore, the structural perturbation theory explains why the theoretical receptivity obtained by the adjoint modes better matches the experimental receptivity for below-natural forcing. The adjoint mode can estimate the receptivity either when the mean flow is not changed by the forcing *at all* or when the forcing *only* acts by changing the mean flow. The latter is hypothesized to not apply to above-natural forcing, but to apply to below-natural forcing.

5 Conclusion

The flow field of a turbulent swirling jet superposed with a PVC as a single-helical global instability in a generic combustion chamber comprising a generic mixing section was investigated. A particular focus was laid on the analysis of the receptivity of the PVC to periodic forcing by theoretical prediction and experimental validation as well as the effect of an actuator onto the flow.

The theoretical receptivity analysis was based on a LSA of the non-actuated turbulent mean flow. The results showed an excellent agreement between predicted and measured frequencies and mode shapes. Subsequently, the adjoint modes of the PVC were calculated. From the magnitude of the adjoint modes it was deduced that the PVC is receptive to periodic open-loop forcing in all velocity components, particularly in a region close to the combustion chamber inlet. Moreover, it was derived that primarily the magnitude of the radial and azimuthal adjoint mode along the centerline are crucial for quantifying the theoretical receptivity of the PVC to the forcing applied by the given ZNMF actuator configuration. The rationale was based on the inspection of the external feedback between the forcing and the PVC mode.

The theoretically derived receptivities were validated by lock-in experiments. In these studies the general trend of decreasing lock-in amplitudes with downstream displaced actuator position was found. Furthermore, the lock-in amplitude increased approximately linearly with increasing difference between forcing and natural frequency. By inverting the linear slope of these lock-in curves the experimental receptivity was quantified and compared to the theoretical receptivity. It was ascertained that the experimental and theoretical receptivity showed a good agreement in the trends, even predicting a local maximum of the receptivity at $x_a/D = -0.75$.

Examining the impact of the actuation, it was shown that the forcing has a significant effect on the mean flow which can definitely not be neglected. For below-natural forcing, PVC lock-in was proven to be primarily reached by a mean flow modification whereas the coherent flow was only marginally modified. This could be interpreted as a phase lock mechanism similar to a VDP oscillator. For above-natural forcing and actuator positions $x_a/D = -2$ and -1.5, the changes to the mean flow were even larger. The PVC amplitude was severely diminished and it was hypothesized that lock-in was reached by a suppression of the natural PVC dynamics that only synchronized to the forcing by a nonlinear mode interaction. As a consequence, one has to be careful in subsequent experiments since an important requirement for the control of the PVC was stated to be that the mean flow is *not* significantly changed. Hence, the mean flow changes should always be monitored when active flow control is applied.

For forcing structures similar to point sources the adjoint modes provide a straightforward method to quantify the receptivity of a global instability mode, such as the PVC, to open-loop control. For a complex, volumetric forcing this is generally not the case. However, when the actual structure of the forcing is known, i.e. the magnitude of each component and its spatial dependence, one can resort to calculating the external feedback within the adjoint LSA framework. This allows for isolating regions where the strongest coupling between forcing and natural mode occurs. This in turn enables to consider a single scalar value of the adjoint at a fixed streamwise position to estimate the true

receptivity of the mode. With structural perturbation theory the results may even be improved. However, one would need to know the actual mean flow modifications caused by the introduced perturbations of the actuator.

For *a priori* propositions when designing actuators or evaluating implementation concepts for these, this may be a problem since the forcing structure or mean flow modifications are not known beforehand. There are some solutions nonetheless in order to use the adjoint modes as a tool for guiding actuator designs. One solution is to use the adjoints as a guide for finding locations that provide a satisfying tradeoff between maximum receptivity and technical feasibility. Subsequently, the actuator would need to be designed such that it is particularly strong in the location and component desired. If the actuator design is predefined to a certain extent (maybe due to technical restrictions), another solution is to characterize this predefined actuator in separate experiments. The findings can then be combined with the adjoint mode to estimate the coupling with the instability mode.

Altogether, this work demonstrated that, in the context of the PVC, the adjoint LSA can be a valuable and valid tool for guiding the process of finding optimal actuator positions and optimal forcing directions without the need of laborious preliminary actuation experiments. This tool will support the definition of optimal actuator designs for active flow control in future studies which investigate the PVC in reacting flows and its quantitative impact on fluid dynamic, thermodynamic, acoustic and structural parameters of the combustion system.

In future studies it would also be important to extend the findings of this work for actuator positions farther downstream, especially close to the exit of the swirling jet where the global maximum receptivity is expected to reside. In this regard, it would also be expedient to test actuator designs with unidirectional forcing to further consolidate the validity of each of the adjoint mode components independently within the open-loop framework. Furthermore, ultimate statements regarding the actual lock-in mechanisms for actuator positions $x_a/D \geq -1$ should be obtained by future experiments to improve our understanding of how synchronization is physically achieved in these cases.

Bibliography

[1] Peckham, D. and Atkinson, S., "Preliminary Results of Low Speed Wind Tunnel Tests on a Gothic Wing of Aspect Ratio, 1.0, Aeronaut," *Res. Counc. Tech. Rep., CP*, no. 508, 1957.

[2] Ligrani, P., "Heat transfer augmentation technologies for internal cooling of turbine components of gas turbine engines," *International Journal of Rotating Machinery*, vol. 2013, 2013.

[3] Syred, N. and Beer, J., "Combustion in swirling flows: a review," *Combustion and flame*, vol. 23, no. 2, pp. 143–201, 1974.

[4] Oberleithner, K., Paschereit, C., and Wygnanski, I., "On the impact of swirl on the growth of coherent structures," *Journal of Fluid Mechanics*, vol. 741, pp. 156–199, 2014.

[5] Moeck, J. P., Bourgouin, J.-F., Durox, D., Schuller, T., and Candel, S., "Nonlinear interaction between a precessing vortex core and acoustic oscillations in a turbulent swirling flame," *Combustion and Flame*, vol. 159, no. 8, pp. 2650–2668, 2012.

[6] Terhaar, S., Ćosić, B., Paschereit, C., and Oberleithner, K., "Suppression and excitation of the precessing vortex core by acoustic velocity fluctuations: An experimental and analytical study," *Combustion and Flame*, vol. 172, pp. 234–251, 2016.

[7] Ghani, A., Poinsot, T., Gicquel, L., and Müller, J.-D., "Les study of transverse acoustic instabilities in a swirled kerosene/air combustion chamber," *Flow, Turbulence and Combustion*, vol. 96, no. 1, pp. 207–226, 2016.

[8] Stöhr, M., Arndt, C. M., and Meier, W., "Transient effects of fuel–air mixing in a partially-premixed turbulent swirl flame," *Proceedings of the Combustion Institute*, vol. 35, no. 3, pp. 3327–3335, 2015.

[9] Terhaar, S., Krüger, O., and Paschereit, C. O., "Flow Field and Flame Dynamics of Swirling Methane and Hydrogen Flames at Dry and Steam Diluted Conditions," *Journal of Engineering for Gas Turbines and Power*, vol. 137, no. 4, p. 041 503, 2015.

[10] Chomaz, J.-M., "Global instabilities in spatially developing flows: non-normality and nonlinearity," *Annu. Rev. Fluid Mech.*, vol. 37, pp. 357–392, 2005.

[11] Gallaire, F., Ruith, M., Meiburg, E., Chomaz, J.-M., and Huerre, P., "Spiral vortex breakdown as a global mode," *Journal of Fluid Mechanics*, vol. 549, pp. 71–80, 2006.

[12] Oberleithner, K., Sieber, M., Nayeri, C., Paschereit, C., Petz, C., Hege, H.-C., Noack, B., and Wygnanski, I., "Three-dimensional coherent structures in a swirling jet undergoing vortex breakdown: stability analysis and empirical mode construction," *Journal of Fluid Mechanics*, vol. 679, pp. 383–414, 2011.

[13] Theofilis, V., "Global linear instability," *Annual Review of Fluid Mechanics*, vol. 43, pp. 319–352, 2011.

[14] Paredes, P., Terhaar, S., Oberleithner, K., Theofilis, V., and Paschereit, C. O., "Global and local hydrodynamic stability analysis as a tool for combustor dynamics modeling," *Journal of Engineering for Gas Turbines and Power*, vol. 138, no. 2, p. 021 504, 2016.

[15] Tammisola, O. and Juniper, M., "Coherent structures in a swirl injector at Re= 4800 by nonlinear simulations and linear global modes," *Journal of Fluid Mechanics*, vol. 792, pp. 620–657, 2016.

[16] Kaiser, T. L., Poinsot, T., and Oberleithner, K., "Stability and Sensitivity Analysis of Hydrodynamic Instabilities in Industrial Swirled Injection Systems," *Journal of Engineering for Gas Turbines and Power*, vol. 140, no. 5, p. 051 506, 2018.

[17] Giannetti, F. and Luchini, P., "Structural sensitivity of the first instability of the cylinder wake," *Journal of Fluid Mechanics*, vol. 581, pp. 167–197, 2007.

[18] Marquet, O., Sipp, D., and Jacquin, L., "Sensitivity analysis and passive control of cylinder flow," *Journal of Fluid Mechanics*, vol. 615, pp. 221–252, 2008.

[19] Meliga, P., Pujals, G., and Serre, E., "Sensitivity of 2-D turbulent flow past a D-shaped cylinder using global stability," *Physics of Fluids (1994-present)*, vol. 24, no. 6, p. 061 701, 2012.

[20] Meliga, P., Boujo, E., and Gallaire, F., "A self-consistent formulation for the sensitivity analysis of finite-amplitude vortex shedding in the cylinder wake," *Journal of Fluid Mechanics*, vol. 800, pp. 327–357, 2016.

[21] Strykowski, P. and Sreenivasan, K., "On the formation and suppression of vortex 'shedding' at low Reynolds numbers," *Journal of Fluid Mechanics*, vol. 218, pp. 71–107, 1990.

[22] Parezanović, V. and Cadot, O., "Experimental sensitivity analysis of the global properties of a two-dimensional turbulent wake," *Journal of Fluid Mechanics*, vol. 693, pp. 115–149, 2012.

[23] Magri, L. and Juniper, M. P., "Global modes, receptivity, and sensitivity analysis of diffusion flames coupled with duct acoustics," *Journal of Fluid Mechanics*, vol. 752, pp. 237–265, 2014.

[24] Kuhn, P., Moeck, J. P., Paschereit, C. O., and Oberleithner, K., "Control of the precessing vortex core by open and closed-loop forcing in the jet core," in *ASME Turbo Expo 2016: Turbomachinery Technical Conference and Exposition*, American Society of Mechanical Engineers, 2016.

[25] Lückoff, F., Sieber, M., Paschereit, C. O., and Oberleithner, K., "Characterization of Different Actuator Designs for the Control of the Precessing Vortex Core in a Swirl-Stabilized Combustor," *Journal of Engineering for Gas Turbines and Power*, vol. 140, no. 4, p. 041 503, 2018.

[26] Crow, S. C. and Champagne, F., "Orderly structure in jet turbulence," *Journal of Fluid Mechanics*, vol. 48, no. 03, pp. 547–591, 1971.

[27] Hussain, A. F., "Coherent structures - reality and myth," *Physics of Fluids (1958-1988)*, vol. 26, no. 10, pp. 2816–2850, 1983.

[28] Reynolds, W. and Hussain, A., "The mechanics of an organized wave in turbulent shear flow. Part 3. Theoretical models and comparisons with experiments," *Journal of Fluid Mechanics*, vol. 54, no. 2, pp. 263–288, 1972.

[29] Cavalieri, A. V., Rodriguez, D., Jordan, P., Colonius, T., and Gervais, Y., "Wavepackets in the velocity field of turbulent jets," *Journal of fluid mechanics*, vol. 730, pp. 559–592, 2013.

[30] Oster, D. and Wygnanski, I., "The forced mixing layer between parallel streams," *Journal of Fluid Mechanics*, vol. 123, pp. 91–130, 1982.

[31] Leibovich, S., "The structure of vortex breakdown," *Annual Review of Fluid Mechanics*, vol. 10, no. 1, pp. 221–246, 1978.

[32] Liang, H. and Maxworthy, T., "An experimental investigation of swirling jets," *Journal of Fluid Mechanics*, vol. 525, pp. 115–159, 2005.

[33] Oberleithner, K., "On Turbulent Swirling Jets: Vortex Breakdown, Coherent Structures, and their Control," PhD thesis, Universitätsbibliothek der Technischen Universität Berlin, 2012.

[34] Barkley, D., "Linear analysis of the cylinder wake mean flow," *Europhys. Lett.*, vol. 75, pp. 750–756, 2006.

[35] Petz, C., Hege, H.-C., Oberleithner, K., Sieber, M., Nayeri, C., Paschereit, C., Wygnanski, I., and Noack, B., "Global modes in a swirling jet undergoing vortex breakdown," *Physics of Fluids*, vol. 23, no. 9, p. 091 102, 2011.

[36] Balanov, A., Janson, N., Postnov, D., and Sosnovtseva, O., *Synchronization: from simple to complex*. Springer Science & Business Media, 2008.

[37] Juniper, M. P., Li, L. K., and Nichols, J. W., "Forcing of self-excited round jet diffusion flames," *Proceedings of the Combustion Institute*, vol. 32, no. 1, pp. 1191–1198, 2009.

[38] Li, L. K. and Juniper, M. P., "Lock-in and quasiperiodicity in a forced hydrodynamically self-excited jet," *Journal of Fluid Mechanics*, vol. 726, pp. 624–655, 2013.

[39] Berkooz, G., Holmes, P., and Lumley, J. L., "The proper orthogonal decomposition in the analysis of turbulent flows," *Annual review of fluid mechanics*, vol. 25, no. 1, pp. 539–575, 1993.

[40] Rukes, L., Paschereit, C. O., and Oberleithner, K., "An assessment of turbulence models for linear hydrodynamic stability analysis of strongly swirling jets," *European Journal of Mechanics-B/Fluids*, vol. 59, pp. 205–218, 2016.

[41] Ivanova, E. M., Noll, B. E., and Aigner, M., "A numerical study on the turbulent Schmidt numbers in a jet in crossflow," *Journal of Engineering for Gas Turbines and Power*, vol. 135, no. 1, p. 011 505, 2013.

[42] Paredes, P., "Advances in global instability computations: from incompressible to hypersonic flow," PhD thesis, Technical University of Madrid, Madrid, Spain, 2014.

[43] Luchini, P. and Bottaro, A., "An introduction to adjoint problems," *Annu. Rev. Fluid Mech., Suppl. Append. A*, vol. 46, pp. 493–517, 2014.

[44] Oden, J. T. and Demkowicz, L., *Applied functional analysis*. CRC press, 2017.

[45] Chandler, G. J., "Sensitivity analysis of low-density jets and flames," PhD thesis, University of Cambridge, 2011.

[46] Welch, P., "The use of fast Fourier transform for the estimation of power spectra: a method based on time averaging over short, modified periodograms," *IEEE Transactions on audio and electroacoustics*, vol. 15, no. 2, pp. 70–73, 1967.

[47] Theofilis, V., Duck, P., and Owen, J., "Viscous linear stability analysis of rectangular duct and cavity flows," *Journal of Fluid Mechanics*, vol. 505, pp. 249–286, 2004.

[48] Khorrami, M. R., Malik, M. R., and Ash, R. L., "Application of spectral collocation techniques to the stability of swirling flows," *Journal of Computational Physics*, vol. 81, no. 1, pp. 206–229, 1989.

[49] Batchelor, G. and Gill, A. E., "Analysis of the stability of axisymmetric jets," *Journal of Fluid Mechanics*, vol. 14, no. 4, pp. 529–551, 1962.

[50] Israeli, M. and Orszag, S. A., "Approximation of radiation boundary conditions," *Journal of computational physics*, vol. 41, no. 1, pp. 115–135, 1981.

[51] Meliga, P., Gallaire, F., and Chomaz, J.-M., "A weakly nonlinear mechanism for mode selection in swirling jets," *Journal of Fluid Mechanics*, vol. 699, pp. 216–262, 2012.

[52] Pope, S. B., *Turbulent flows*. IOP Publishing, 2001.